WL-TR-92-4111

THE DEFORMATION OF NIAL BICRYSTALS

DANIEL B. MIRACLE

MATERIALS DIRECTORATE
WRIGHT LABORATORY
AIR FORCE SYSTEMS COMMAND
WRIGHT PATTERSON AFB OH   45433- 7734

JUN 1990

FINAL   REPORT FOR 06/01/85-06/30/90

DTIC
APR 19 1993
S   B   D

93-07991

‖‖‖‖‖‖‖‖‖‖‖‖‖‖

MATERIALS DIRECTORATE
WRIGHT LABORATORY
AIR FORCE SYSTEMS COMMAND
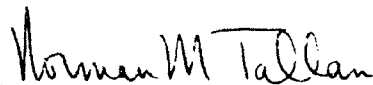WRIGHT PATTERSON AFB OH 45433- 7734

NOTICE

WHEN GOVERNMENT DRAWINGS, SPECIFICATIONS, OR OTHER DATA ARE USED FOR ANY PURPOSE OTHER THAN IN CONNECTION WITH A DEFINITELY GOVERNMENT-RELATED PROCUREMENT, THE UNITED STATES GOVERNMENT INCURS NO RESPONSIBILITY OR ANY OBLIGATION WHATSOEVER. THE FACT THAT THE GOVERNMENT MAY HAVE FORMULATED OR IN ANY WAY SUPPLIED THE SAID DRAWINGS, SPECIFICATIONS, OR OTHER DATA, IS NOT TO BE REGARDED BY IMPLICATION, OR OTHERWISE IN ANY MANNER CONSTRUED, AS LICENSING THE HOLDER, OR ANY OTHER PERSON OR CORPORATION; OR AS CONVEYING ANY RIGHTS OR PERMISSION TO MANUFACTURE, USE, OR SELL ANY PATENTED INVENTION THAT MAY IN ANY WAY BE RELATED THERETO.

THIS REPORT HAS BEEN REVIEWED BY THE OFFICE OF PUBLIC AFFAIRS (ASD/PA) AND IS RELEASABLE TO THE NATIONAL TECHNICAL INFORMATION SERVICE (NTIS). AT NTIS IT WILL BE AVAILABLE TO THE GENERAL PUBLIC INCLUDING FOREIGN NATIONS.

THIS TECHNICAL REPORT HAS BEEN REVIEWED AND IS APPROVED FOR PUBLICATION.

DANIEL B. MIRACLE
Project Engineer

NORMAN M. TALLAN, Chief
Metals & Ceramics Division
Materials Directorate

IF YOUR ADDRESS HAS CHANGED, IF YOU WISH TO BE REMOVED FROM OUR MAILING LIST, OR IF THE ADDRESSEE IS NO LONGER EMPLOYED BY YOUR ORGANIZATION PLEASE NOTIFY WL/MLLM , WRIGHT-PATTERSON AFB, OH 45433-7734 TO HELP MAINTAIN A CURRENT MAILING LIST.

COPIES OF THIS REPORT SHOULD NOT BE RETURNED UNLESS RETURN IS REQUIRED BY SECURITY CONSIDERATIONS, CONTRACTUAL OBLIGATIONS, OR NOTICE ON A SPECIFIC DOCUMENT.

REPORT DOCUMENTATION PAGE

Public reporting burden for this collection of information is estimated to average 1 hour per response, including the time for reviewing instructions, searching existing data sources, gathering and maintaining the data needed, and completing and reviewing the collection of information. Send comments regarding this burden estimate or any other aspect of this collection of information, including suggestions for reducing this burden, to Washington Headquarters Services, Directorate for information Operations and Reports, 1215 Jefferson Davis Highway, Suite 1204, Arlington, VA 22202-4302, and to the Office of Management and Budget, Paperwork Reduction Project (0704-0188), Washington, DC 20503.

1. AGENCY USE ONLY (Leave blank)	2. REPORT DATE	3. REPORT TYPE AND DATES COVERED	
	JUN 1990	FINAL	06/01/85--06/30/90

4. TITLE AND SUBTITLE THE DEFORMATION OF NIAL BICRYSTALS

5. FUNDING NUMBERS
C
PE   61102
PR   2306
TA   P1
WU   06

6. AUTHOR(S) DANIEL B. MIRACLE

7. PERFORMING ORGANIZATION NAME(S) AND ADDRESS(ES)

MATERIALS DIRECTORATE
WRIGHT LABORATORY
AIR FORCE SYSTEMS COMMAND
WRIGHT PATTERSON AFB OH 45433- 7734
WL/MLLM, ATTN: MIRACLE (513)255-9833

8. PERFORMING ORGANIZATION REPORT NUMBER

WL-TR-92-4111

9. SPONSORING/MONITORING AGENCY NAME(S) AND ADDRESS(ES)

10. SPONSORING/MONITORING AGENCY REPORT NUMBER

11. SUPPLEMENTARY NOTES

12a. DISTRIBUTION/AVAILABILITY STATEMENT
APPROVED FOR PUBLIC RELEASE; DISTRIBUTION IS UNLIMITED.

12b. DISTRIBUTION CODE

13. ABSTRACT (Maximum 200 words)

The glide of non-<100> dislocations at NiAl grain boundaries is proposed to account for the observed ductility of this compound near the brittle-to-ductile transition temperature. Two bicrystal orientations have been produced to investigate the activation of <111> dislocations due to the concentrated local stress at the bicrystal interface arising from elastic and plastic incompatibility. Observations of surface slip markings and TEM characterization of the dislocations responsible for bicrystal deformation have been made.

The glide of <110> dislocations on {110} planes is the dominant mode of deformation in the vicinity of the oriented bicrystal interfaces investigated. It is concluded that the glide of non-<100> dislocations may contribute to the plasticity of polycrystalline NiAl in a general sense, and not just in cube-oriented single crystals where <100> slip is geometrically restricted. The dominant mode of <110> dislocation generation is the nucleation of <110> loops away from the

14. SUBJECT TERMS NIAL, NICKEL ALUMINIDE, BICRYSTAL, DEFORMATION, DISLOCATION STRUCTURES, STRESS CONCENTRATION

15. NUMBER OF PAGES
111

16. PRICE CODE

17. SECURITY CLASSIFICATION OF REPORT	18. SECURITY CLASSIFICATION OF THIS PAGE	19. SECURITY CLASSIFICATION OF ABSTRACT	20. LIMITATION OF ABSTRACT
UNCLASSIFIED	UNCLASSIFIED	UNCLASSIFIED	UL

NSN 7540-01-280-5500

grain boundary. The macroscopic stress required to activate these <110> dislocations, in the presence of a stress concentration such as that produced by a dislocation pile-up at a grain boundary, is the same as that required to nucleate <100> dislocations. The statistical relevance of this phenomenon as it pertains to the general deformation of NiAl polycrystals has not been established.

The movement of <100> dislocations provides the primary mode of deformation for cube-oriented single crystals. A climb force exists on [001] dislocations in a crystal stressed along the [001] axis, but a continuous source of vacancies is required for the extensive motion of these dislocations. It is suggested that the climb of [100] and [010] dislocations provides the required vacancies, and that the gradient in the concentration of vacancies provides the driving force for the motion of these dislocations. The climb of dislocations due to diffusion along dislocation cores is shown to allow for a significant enhancement of the strain rate due to the climb of <100> dislocations.

FOREWORD

The research described herein was performed through financial support provided by the Air Force Office of Scientific Research and in facilities of the Processing and High Temperature Materials Branch (MLLM), Materials Directorate (formerly Materials Laboratory), Air Force Wright Laboratory (formerly Wright Research and Development Center) at Wright-Patterson Air Force Base, OH. The reserach was conducted during the period of June 1985 through May 1990. I am grateful to the many friends and coworkers who have shared their time and talents during the course of this research project. Special gratitude is due to Dr. Ram Darolia at the General Electric Aircraft Engine Business Group, who supplied the single crystal material for this work. Dr. Darolia openly shared his data, which appears in Fig. 2, and has helped with many intriguing questions posed during discussions. I would also like to thank Dr. Dennis Dimiduk, who has provided insight and inspriation through several discussions,. I would like to express my gratitude to Jerry Barlow, Tim Campbell, George Cornish, and Bob Lewis for help in specimen preparation, and to Scott Apt for electropolishing the TEM foils. Special thanks are also due to Judy Paine and Cheryl Heidenreich for assistance with the photographic plates, to John Roberts for assistance concerning Fortran programming, and to Prof. Raghavan Srinivasan at Wright State University for assistance with the MTS machine during diffusion bonding.

The thoughtful comments from members of the thesis committee are especially acknowledged. Discussions with Dr. J. P. Hirth throughout the course of this work have been of great assistance regarding the fine points of elastic and plastic constraints at grain boundaries. I would like to thank Prof. William Clark for critical comments concerning the electron microscopy and for assistance with definition of the grain boundary crystallography. Prof. Hamish Fraser provided comments and discussions which have significantly shaped the thoughts followed in this work.

TABLE OF CONTENTS

LIST OF TABLES

LIST OF FIGURES

LIST OF SYMBOLS

A list of the symbols used is given below. Symbols modified with a subscript A or B refer to crystal A or crystal B in a bicrystal specimen, respectively. A "primed" symbol indicates reference to the grain boundary coordinate axes defined for bicrystal specimens in Section 3.2.1. The terms "appl", "elas", and "plas", either as a subscript or a superscript, refer to stress and strain components due to the macroscopically applied stress, elastic incompatibility, and plastic incompatibility in a deformed bicrystal sample, respectively. A subscript p or a (p) refers to the pth slip system in crystal A.

A	*constant*
$\mathcal{A}$	Zener elastic anisotropy constant
a_0	lattice constant
b	Burgers vector
$b(i)$, b_i	i^{th} component of **b**
|b|	magnitude of the Burgers vector
C_{ij}, C_{ijkl}	elastic compliance tensor
D	bulk diffusion coefficient
D_c	diffusion coefficient along dislocation cores
$\Delta l/l_0$	coefficient of thermal expansion
ΔH	activation energy
ε	engineering strain
$\dot{\varepsilon}$	strain rate
F/L	force per unit length along a dislocation line

Φ	Schmid factor
G	shear modulus
$\mathbf{g}$	diffraction vector in TEM analysis
$|g|$	magnitude of diffraction vector $\mathbf{g}$
$\mathbf{i}$	unit vector along the x-axis
$\mathbf{j}$	unit vector along the y-axis
$\mathbf{k}$	unit vector along the z-axis
K	constant
k	Boltzmann constant
l/d	aspect ratio of a compression sample
λ	wavelength of electrons
m	strain-rate hardening exponent from the relation $\dot{\epsilon}=K\sigma^m$
$\mathbf{n}$	slip plane normal
$n(i)$	i^{th} component of $\mathbf{n}$
n	order of reflection satisfying the Bragg condition in weak beam
n	strain hardening exponent from the relation $\sigma=K\epsilon^n$
P	applied stress
π	pi
RT	room temperature
r_0, r	inner and outer cutoff radii for calculation of dislocation line energy
S_{ij}, S_{ijkl}	elastic stiffness tensor
s_g	deviation parameter
σ_{ij}	components of the stress tensor
T	absolute temperature
T_m	melting temperature
τ	resolved shear stress
$\tau_{crss}^{<100>}$	critical resolved shear stress for <100> slip

$\tau_{crss}^{<110>}$ critical resolved shear stress for <110> slip

$\tau_{crss}^{<111>}$ critical resolved shear stress for <111> slip

$\mathbf{u}$ dislocation line vector

u_i i^{th} component of $\mathbf{u}$

$\mathbf{w}$ $(\xi_g)(s_g)$

$\mathbf{x}_1', \mathbf{x}_2', \mathbf{x}_3'$ grain boundary coordinate axes

ξ_g effective extinction distance for reflection $\mathbf{g}$

CHAPTER I

INTRODUCTION

As a class of materials, ordered intermetallic compounds possess a wide range of unique and useful characteristics, including the well-known shape-memory effect (NiTi), exceptional superconducting properties (Nb_3Sn), the unique capability of solid-state laser action (GaAs), excellent magnetic coercive force (FePt), and the anomalous dependence of yield stress on temperature (Ni_3Al). Ordered intermetallic compounds also typically exhibit high moduli, very slow rates of diffusion, and good strength retention at high homologous temperatures, all desirable characteristics for high temperature structural materials. Currently, however, the primary role of intermetallic compounds in structural materials is as a precipitated second phase in Ni-base superalloys, high strength aluminum alloys, and a few specialty steels. The primary barrier to the implementation of ordered alloys as monolithic structural materials is the lack of sufficient ductility and damage tolerance at room temperature.

The Ni-aluminide NiAl offers significant promise for high temperature applications due to its good strength and high melting temperature. NiAl exhibits limited plasticity below 300 °C in single crystal form, and shows little or no ductility below 400 °C in polycrystalline form. Above 400 °C, both single crystals and polycrystals of NiAl possess significant ductility. Only three independent slip systems are favored to operate in polycrystalline NiAl below 400 °C, and this fact has been used to explain the lack of ductility in NiAl. Above the ductile-to-brittle transition temperature (DBTT), slip is presumed to be limited to the same three slip systems, so that the mechanism by which polycrystalline NiAl may deform plastically is not clear. The only mechanism proposed to

1

account for the plasticity of NiAl, the stress-assisted diffusional climb of dislocations, has not been shown in the open literature rigorously to account for the observed behavior.

A strong effort to alter the plastic behavior of NiAl through alloying and microstructural control is evident in the current literature, yet the basic mechanisms which govern the mechanical response of the binary compound are not understood. The overall objective of this thesis is therefore to investigate the mechanism by which polycrystalline NiAl is able to deform plastically above the DBTT. In particular, the possibility of additional slip systems becoming active at stress concentrations, such as grain boundaries, will be addressed. The physical characteristics of NiAl which are pertinent to this investigation are presented in the following chapter, along with a review of the operative modes of deformation for both single crystal and polycrystalline NiAl. A critical analysis of the mechanism previously proposed to account for the plasticity of NiAl is presented in Chapter III, along with the development of an alternate theory to explain the observed mechanical response of NiAl. An experimental program to investigate the validity of this new theory is described in Chapters IV and V, and the results are given in Chapter VI. A discussion of the results (Chapter VII) and suggestions for future research concludes this thesis project.

CHAPTER II

BACKGROUND

2.1 Physical Properties

NiAl is iso-structural with CsCl, and remains ordered to its melting temperature of 1638 °C. The symmetry is primitive cubic (Pearson symbol cP2), but the structure is related to the bcc lattice, with one atom type occupying cube corners and the other atom type at the cube center, as shown in Fig. 1. NiAl is elastically anisotropic, with a Zener anisotropy factor, given by

$$\mathcal{A} = 2(C_{44})/(C_{11}-C_{12}) \tag{1}$$

of 3.28 at room temperature ($\mathcal{A}$=1.20 for Cu and 8.49 for β-CuZn) [1]. The Frank criterion, which states that the line energy of a dislocation is proportional to the square of its Burgers vector, suggests that dislocations with the 1/2<111> vector are preferred, as commonly observed in bcc metals. However, this translation results in a plane of atoms occupying the wrong site in the ordered lattice after the passage of such a dislocation, and a second 1/2<111> dislocation is required to restore symmetry. The Ni-Al bond energy in NiAl is high (~ 0.08 eV/bond), and the resulting anti-phase boundary (APB) energy between the leading and trailing 1/2<111> partial dislocations is therefore expected to be high. First principles calculations utilizing an all-electron total energy band structure calculation have estimated this APB energy to be ~900 ergs/cm^2 [2]. If this dislocation arrangement is stable, the separation between the leading and trailing 1/2<111> partial dislocations is calculated to be ~0.4 nm for screw dislocations and ~0.6 nm for edge dislocations, and overlap of the inelastic strain fields of the partial dislocation cores is not expected to allow the two partial dislocations to be resolved by electron microscopy. In

3
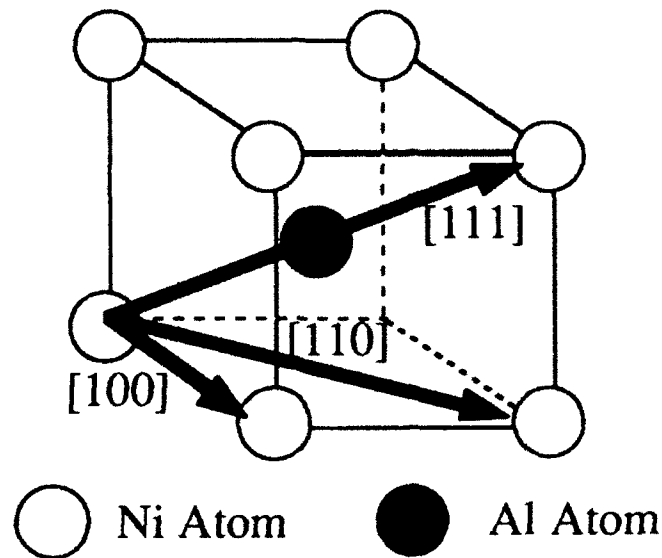
Figure 1. The CsCl crystal structure. Three Burgers vectors representing the <100>, <110>, and <111> perfect dislocations observed in NiAl are shown by the arrows.

agreement with this analysis, the separation of <111> dislocations into two stable

1/2<111> partial dislocations has not been experimentally observed. The three unit

translation vectors [100], [110], and [111] shown in Fig. 1 define the shortest lattice

translations that do not disturb the order of the crystal. Perfect dislocations corresponding

to each of these translations have been observed in deformed NiAl, although the <110> and

<111> vectors are typically seen only in single crystals subjected to uniaxial loading along

a <100> direction, as will be discussed in detail in the next section.

2.2 Deformation and Mechanical Behavior of NiAl

A review of the mechanical behavior and deformation mechanisms of NiAl is

presented to provide the background for a development of the mechanism responsible for

the plasticity in polycrystalline NiAl. Deviations from the equiatomic composition exert a

profound influence on many aspects of deformation in NiAl, however, these effects will

not be considered in the present work, and the literature reviewed will be restricted to stoichiometric NiAl unless stated otherwise. Investigations on single crystals will be emphasized since the relationship between the applied state of stress and the resulting deformation microstructure is better controlled and understood. However, observations on polycrystals are essential to the understanding of the mechanism of ductility in NiAl, and will be presented. Although a number of techniques and observations have been applied in the literature to deduce the slip vector in deformed specimens, special emphasis is given to transmission electron microscopy (TEM) determinations employing two or more $g \cdot b = 0$ invisibility conditions. Deformation under creep conditions will not be discussed.

Common to all investigations on NiAl is the absence of planar defects such as APB's and stacking faults. Similarly, other deformation modes, such as twinning, have not been observed for alloys near the stoichiometric composition (note that the ordered $L1_0$ martensite occurs only for Ni-rich NiAl [3]). Finally, only perfect dislocations have been observed to be stable in NiAl. In only one case has a <111> dislocation image been resolved into two superlattice partial dislocations, however, post-deformation analysis showed no separation of the <111> dislocations, and a subsequent anneal was required to reveal a separation of the edge segments [4]. Calculations of the elastic energy of <111> edge dislocations at room temperature (RT) [5] show that they are elastically unstable, and are expected to decompose into the elastically stable <100> and <110> reaction products (also, see Fig. 17). No attempt was made by Campany et al. to differentiate between the separation into two 1/2<111> superlattice partial dislocations and the elastically stable <100>+<110> reaction products expected to occur.

2.2.1 Single Crystals

The deformation and mechanical behavior of NiAl single crystals is strongly dependent upon crystal orientation. A sharp contrast is observed between crystals tested along a <100> axis, denoted as "hard" crystals in the literature, and crystals tested along a

non-<100> direction, referred to as "soft" crystals. These two classes of orientations will be discussed separately.

2.2.1.1 "Soft" Single Crystals

The mechanical behavior of "soft" single crystals has been investigated in both tension and compression for a number of orientations over a wide temperature range. The yield stress is seen to decrease rapidly from -196 °C to RT, and is relatively constant or drops slowly with increasing temperature from RT to 871 °C [6-10]. The flow stress is often reported to be strongly temperature dependent above 600 °C, but this is most pronounced in polycrystals and non-stoichiometric single crystals, and is not a trend for stoichiometric "soft" single crystals. Large plastic strains are often reported, however, the majority of the results have been obtained in compression. Significant tensile ductility is obtained at 200 °C and above [6], but tensile plastic strain at RT is typically less than 1% [9,10]. The transition from elastic deformation to plastic flow generally occurs smoothly, but large, irregular load drops are observed for single crystals tested in compression at RT along a <123> compression axis [6]. Each load drop corresponds to the formation of a visible deformation band, which spreads laterally between load drops. Load drops are not observed in <123> specimens tested in tension at RT [10].

An analysis of the operative slip system based on observations of surface slip markings reveals that the slip vector is <100> over the entire temperature range investigated [6,11]. The active slip planes for [110] crystals are reported to be (100) and (010) between 200 °C and 700 °C [6], and this is corroborated by the results of Pascoe and Newey above 600 °C [11]. In addition, the slip plane is determined to be (010) for [110] single crystals at RT, and (110) at -196 °C [11]. All other orientations generally exhibit a {110} slip plane, but Pascoe and Newey [11] and Ball and Smallman [12] also report cross-slip onto higher index planes of a <100> zone, such as (210). However, Ball and Smallman contend that these apparent higher-order index slip traces are the manifestation of pencil

6

glide, or cross-slip onto orthogonal {110} slip planes.

Contrast experiments using TEM have shown that the primary Burgers vector is <100> [12,13], in agreement with the conclusions drawn from surface slip markings. Ball and Smallman required several foils cut from different orientations in the specimen for a complete analysis, presumably due to limited tilt available with the specimen stage. It is important to note that different dislocation morphologies are observed in the various micrographs used to deduce the slip vector. The dislocations in Fig. 5(a) and Fig. 5(b) of Ball and Smallman show long dislocations that are heavily pinned along their length, while the dislocations in Fig. 6(a) and Fig. 6(b) are typically short and straight. This may simply be a sectioning effect, but this possibility is not discussed by the authors. In addition, dislocations showing different contrast from the majority of the dislocations in Fig. 6(a) and Fig. 6(b) are observed, and these may be other <100> dislocations, <110> dislocations, or <111> dislocations. Again, this is not discussed by Ball and Smallman. Loretto and Wasilewski tersely state that primary and secondary <100> dislocations are observed, but do not present details. However, it may be considered established that NiAl "soft" single crystals deform by the motion of <100> dislocations based on the agreement between TEM experiments and the observations of surface slip markings just discussed. The critical resolved shear stress for <100> slip ($\tau_{crss}^{<100>}$), calculated by resolving the flow stress onto either the observed slip system or the most highly-stressed <100>{110} slip system, is shown as a function of temperature from several investigations [2,6-10] in Fig. 2(a). Bowman et al. have shown that it is useful to consider deformation to occur by a thermally activated process, where the data fit the relation

$$\tau = (A)\exp(-\Delta H/kT) \qquad (2)$$

where τ is either the flow stress or the resolved shear stress, A is a constant, ΔH is the activation energy, k is Boltzmann's constant, and T is the absolute temperature. The data in Fig. 2(a) is plotted as the log of the critical resolved shear stress vs. 1/T in Fig. 2(b).
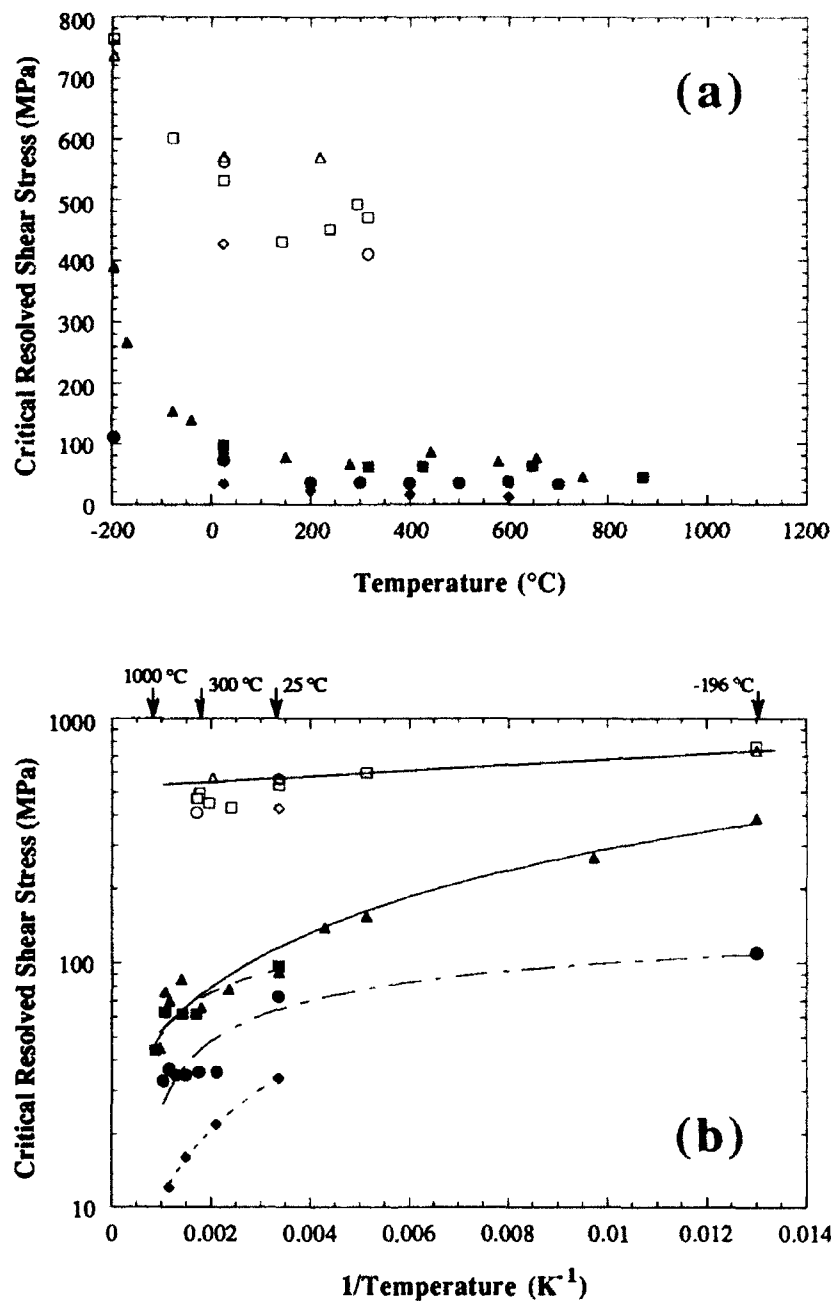
Figure 2. Critical resolved shear stress as a function of temperature for <100>{110} slip in "soft" crystals from (●) Wasilewski et al. [6], (◆) Ball and Smallman [7], (▲) Pascoe and Newey [8], and (■) Lahrman et al. [9]; and for <111>{110} slip in "hard" crystals from (□) Pascoe and Newey [8], (○) Darolia et al. [2], (△) Bowman et al. [10], and (◊) Wasilewski et al. [6]. The data is plotted as (a) τ vs. T and as (b) log(τ) vs. 1/T.

Below 0.45 T_m (600 °C), dislocations are often observed to be heavily pinned, and dislocation tangling, loops, and dipole formation are typically observed [12]. The obstacles responsible for the pinning of the dislocations have not been identified. Ni-rich clusters [14] and locally ordered defects [15] have been proposed to occur in NiAl, but these occur primarily away from the stoichiometric composition. Other possibilities include local ordering of vacancies [16] and divacancy defects [17]. Above 600 °C, dislocation networks and sub-boundaries are typically observed [12]. Planar defects such as APB's and stacking faults, separation of the perfect <100> or <111> dislocations into superlattice partial dislocations, and other modes of deformation, such as twinning, have not been observed in stoichiometric "soft" single crystals.

Very little information is available concerning the fracture behavior of "soft" single crystals. Wasilewski et al. state that "soft" single crystals tested in tension between 200 °C and 400 °C generally exhibit large uniform elongations prior to necking and fracture. Above 400 °C, tensile instability typically results in a knife-edge fracture morphology. This instability is characterized by intensely localized deformation in narrow bands which often occur along the primary slip plane. Secondary slip is observed between these primary slip bands, and the primary slip bands appear to be effective barriers to the propagation of secondary slip. Microcracks are often seen to nucleate at slip band intersections. Extensive, convincing documentation of these results is provided by optical and replica electron microscopy. Pascoe and Newey report that single crystals typically fail by cleavage on {110} planes, but do not provide the data leading to this conclusion [8].

2.2.1.2 "Hard" Single Crystals

2.2.1.2.1 Uniform Deformation

Single crystals tested along one of the cube axes, referred to as "hard" crystals, show flow stresses many times higher than the stress required for the deformation of non-<100>, or "soft", crystals, since there is no macroscopic resolved shear stress on slip
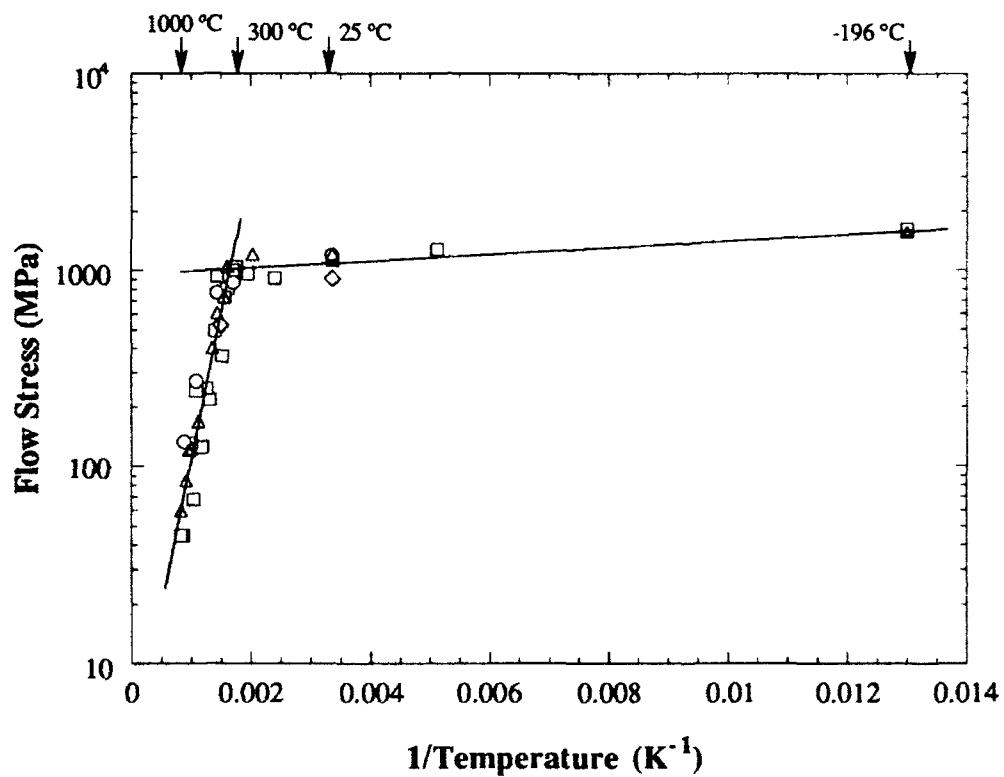
Figure 3. Flow stress as a function of temperature for "hard" crystals from (□) Pascoe and Newey [8], (O) Darolia et al. [2], (Δ) Bowman et al. [10], and (◊) Wasilewski et al. [6].

systems with <100> dislocations. The flow stress as a function of temperature reported in several investigations is shown in Fig. 3 [2,6,8,10]. The deformation of cube-oriented single crystals is nearly temperature independent below 300 °C, but becomes strongly dependent on temperature above this temperature. "Hard" single crystals tested in tension fail elastically at RT and 316 °C, but exhibit uniform elongations which increase rapidly from 20% at 400 °C to nearly 90% at 871 °C [2,6]. One or more necks are formed before reaching the maximum load [6]. A yield drop is observed at 427 °C and 649 °C, but is absent at 871 °C [2]. In compression, <100> crystals often deform by an extremely localized process termed kinking, which occurs over a wide range of temperatures and strain rates [2,6,7,11,18]. Kinking is characterized by sharp load drops occurring in a jerky, irregular manner, and the formation of a single band of deformation which occurs on a plane whose normal is ~20° from the compression axis.

Surface slip markings provide little information on the operative slip system in "hard" crystals. At -196 °C, slip markings are clear but coarse and wavy [13], and slip lines are either absent or indefinite at RT and above [6,11,13,18]. Pascoe and Newey conclude from an analysis of surface slip markings that <111> dislocations are responsible for the deformation of <100> crystals tested at temperatures up to 727 °C, and that the s.ip planes are of the {123} type at -196 °C, and are either {112} or {110} above 600 °C [11]. However, duplex slip and the wavy or indefinite nature of the slip lines complicated this analysis. Slip markings on one face could not be matched with traces on an adjacent orthogonal face, and so the analyses provided by these authors is actually a single surface slip trace analysis. Therefore, these results must be considered as incomplete and inconclusive.

TEM investigations have been carried out to determine the mechanism of deformation in "hard" single crystals. Loretto and Wasilewski report that deformation at -196 °C and RT results from the activation of <111> dislocations, and image simulation shows that the dislocations are perfect dislocations, and are not 1/2<111> [13]. Only very

short edge segments were observed, and an accurate trace analysis was difficult, but suggested a slip plane near {110} or {112}. A slip plane was also deduced from a band of <111> screw dislocations viewed end-on after deformation at -196 °C. The plane defined by the cross product of the slip band trace and the Burgers vector was (154). The reported precision of this measurement led Loretto and Wasilewski to conclude that the slip plane was essentially non-crystallographic, and was not the (011) plane. In agreement with the observations of Loretto and Wasilewski, Bowman et al. report that <111>{112} is the operative slip system for "hard" crystals compressed from -196 °C to 300 °C [10]. However, these authors do not present the details of their TEM investigations.

There are, however, conflicting reports of the operative slip vector in <100> crystals deformed below 300 °C. Fraser et al. [18] and Darolia et al. [2] observe primarily <100> dislocations after deformation below this temperature. Very few <110> and <111> dislocations were observed, and were seen as short, straight segments occurring only at dislocation nodes. These non-<100> segments were adequately explained as the elastically stable reaction products between mobile <100> dislocations.

Each of the TEM investigations of "hard" crystals deformed above 300 °C report only <100> dislocations [2,10,18]. The glide of <100> dislocations in a cube-oriented single crystal is difficult to rationalize, since there is no macroscopic resolved shear stress on these dislocations, but a viable mechanism for the glide of <100> dislocations above 300 °C has not been proposed. However, the observed <100> dislocations may be dislocations which move by diffusion-assisted climb processes, and this will be discussed in the following chapter and in Chapter VII.

The critical resolved shear stress for the glide of <111> dislocations is shown in Fig. 2(a) and Fig. 2(b) from the work of Bowman et al.at -196 °C to 300 °C, and the data occurs on the straight line in Fig. 2(b). Data from other investigations reporting mechanical properties for "hard" crystals below 300 °C are also included, even though <111> slip was not observed in these studies [2,6,8]. The shear stress resolved on the

most favored <111>{110} slip system from these investigations is reasonably close to the critical shear stress calculated from the data of Bowman et al. It is important to note that <111> dislocations are extremely difficult to move, and the critical resolved shear stress for <111> slip at RT amounts to nearly 2% of the shear modulus! A resolved shear stress for the deformation of <100> crystals above 300 °C cannot be calculated, since only <100> dislocations are observed, and the resolved shear stress for these slip systems is zero.

Other details of the deformation microstructures from TEM investigations after uniform deformation show that a large number of long, straight screw dislocations are observed at RT, with a significant number of irregular edge segments, and the edge segments are shorter and far less common at -196 °C [6]. Based on the relative frequency of their occurrence, the edge segments are likely to be more mobile than the screw segments, and this difference is more pronounced at -196 °C. The edge segments are heavily jogged at both temperatures, and these authors suggest that the screw segments cross-slip frequently. Loretto and Wasilewski note that easy cross-slip of the [1$\bar{1}$1] dislocations onto the (011) and (121) slip planes is consistent with the observation of the (154) slip trace[13]. Finally, deformation is observed to be very inhomogeneous, and large regions of the foils investigated by these authors contained no dislocations at all. Areas where the dislocation density was high showed dislocation debris in the form of loops. "Hard" crystals deformed at 550 °C show a high density of prismatic <100> loops [18], and dynamic recrystallization is reported to occur during deformation at 871 °C [2]. Darolia et al. note that the same general features are observed for samples deformed in tension and compression.

2.2.1.2.2   Kinking

Kinking, a severely localized mode of deformation, is often observed in "hard" crystals tested in compression. Although typically observed from RT to ~600 °C [7,11], it has been shown that kinking competes with uniform deformation and may be induced at

higher temperatures by deforming at higher strain rates [18]. Analyses based on observations from optical microscopy, x-ray pole figures, and TEM show that deformation in the kinked band occurs on {110} planes primarily by the motion of the particular <100> dislocations aligned with the compression axis [18,19]. However, all three <100> dislocations are observed in the kink band, along with a small number of short <110> dislocations. Deformation is contained within a band whose normal is ~20° from the compression axis, and rotations of ~60° are observed about a <110> direction which is initially perpendicular to the compression axis. Outside the kinked region, deformation has been reported to be identical to uniformly deformed samples [18] and undeformed samples [2]. Kinking is not observed in tension.

It has recently been proposed that the aspect ratio of test specimens controls the mode of deformation in cube-oriented single crystals compressed below 300 °C [10]. When the aspect ratio is ~3, kinking is always seen to occur [2,11], and when the aspect ratio is ~2, deformation typically occurs by the motion of <111> dislocations [10,13]. The work of Fraser et al., where kinking was observed during the compression of "hard" crystals with an ℓ/d of 2, is the only exception to this generalization [18]. Bending stresses in specimens with an ℓ/d of ~3 are suspected to result in the activation of <100> slip, since elastic bending, or buckling, of planes initially parallel to the compression axis may occur due to the large normal loads and frictional end constraints. These regions of elastic bending may provide a local crystal inhomogeneity which serves as the initiation site for kinking. A small deviation from the <100> axis will greatly increase the possibility of buckling. Further, it can be shown by a simple calculation that a rotation of only 4° from the cube orientation toward a <111> axis may result in the activation of <100> slip in the bulk of the crystal at RT (Fig. 4). Therefore, even a small angular deviation from the cube orientation may result in the activation of <100> slip and kinking. Specimens with an aspect ratio of ~2 are subjected to a more highly constrained state of stress, which might be presumed to favor activation of <111> dislocations, but it is not clear why this constrained

14
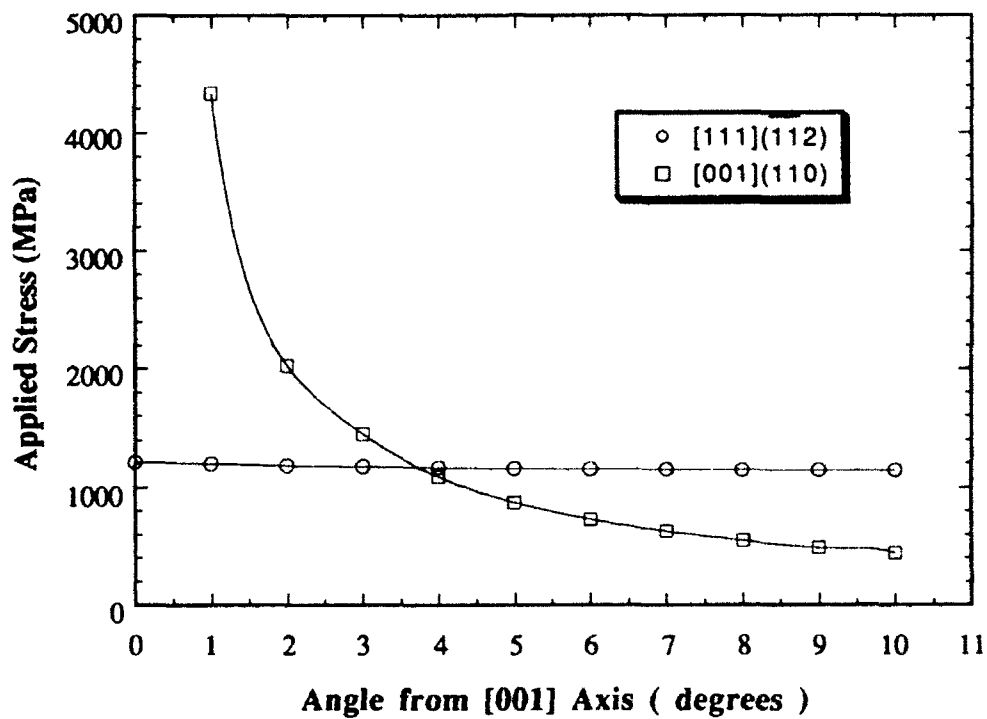
Figure 4. The applied stress required to activate <111> and <100> slip as a function of the misorientation angle from the [001] axis. The stress axis is tilted toward the [111] axis. The critical resolved shear stress for <111> slip is taken to be 571 MPa at RT, and a value of 75 MPa is used for the critical resolved shear stress for <100> slip.

state of stress should favor <111> slip over <100> slip. However, a smaller aspect ratio clearly results in a greatly reduced bending moment for crystals tilted from the <100> direction. Therefore, the observation of <111> dislocations in "hard" crystals is a strong indication that this is the preferred mode of deformation for this orientation, while <100> dislocations and kinking may result from extrinsic effects, and may not be representative of the intrinsic deformation characteristics of perfectly aligned cube-oriented single crystals.

2.2.2 Polycrystals

A remarkable variation in the mechanical behavior of polycrystalline NiAl is evident in the studies reported in the open literature, especially with regard to the strength and ductility as a function of temperature. Brittle failure is reported from RT to ~400 °C in both tension [20,21] and compression [7]. However, documentation of plastic behavior in the same temperature range also exists for tensile [22-24] and compressive [8] deformation. In every study, however, the ductility increases dramatically above 400-600 °C, and this is commonly agreed to be the ductile-to-brittle transition temperature for polycrystalline NiAl. The yield stress of polycrystalline NiAl is shown in Fig. 5 from these investigations. Note that the data of Pascoe and Newey suggest thermally activated deformation from -196 °C to ~300 °C, similar to the behavior of "soft" single crystals, while the data of Rozner and Wasilewski indicates that deformation is athermal in the same temperature range. Significant variation in the magnitude of the yield stress is evident from one investigation to another, and this lack of consistency may be due to differences in grain size, interstitial content, texture from thermomechanical processing, and chemistry. Even qualitative comparisons are difficult, since these important parameters are often not reported in these investigations. Stress-rupture data is provided in only one investigation [20].

Yield drops are often reported [8,23,24], and Pascoe and Newey show by strain aging that pinning due to dislocation "atmospheres" is responsible for this behavior below RT. NiAl shows no strain rate sensitivity at RT, but strain rate change tests indicate that
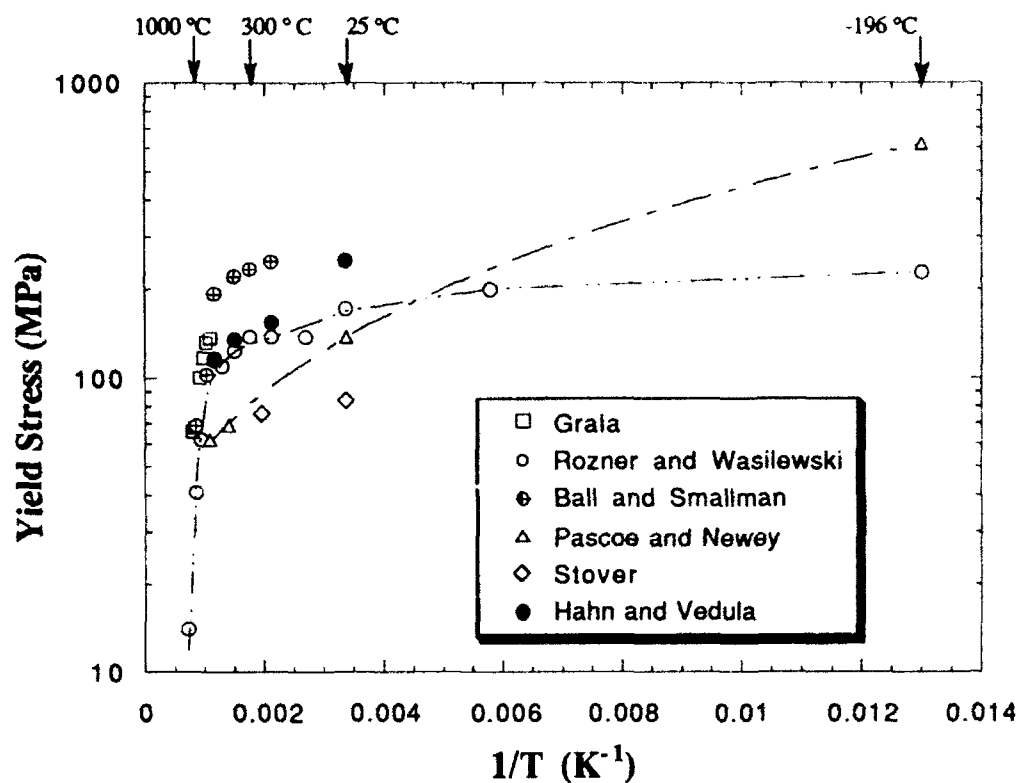
Figure 5. Log(σ_y) vs. 1/T for polycrystalline NiAl from (□) Grala [20], (O)Rozner and Wasilewski [23], (⊕) Ball and Smallman [7], (△) Pascoe and Newey [8], (◊) Stover [22], and (●) Hahn and Vedula [24].

the strain rate sensitivity increases at higher temperatures [23], suggesting that thermally activated processes may be contributing to deformation. Non-uniform deformation is often observed, and is reported as localized deformation at grain boundaries [7] and as striations occurring in bands nearly perpendicular to the compression axis [25]. Widely different dislocation densities are also observed from one region to another in TEM [26]. Stable cracking is reported in both tension [20] and compression [25]. However, stable cracking is absent in the work of Hahn and Vedula. The mode of fracture is reported to be primarily intergranular at RT, with an increasing contribution of transgranular fracture at higher temperatures [24]. At 600 °C, failure occurs by microvoid coalescence and ductile rupture [24,27]. Pascoe and Newey report that the fracture mode is typically intergranular for material with a grain size of 50 μm, but the incidence of transgranular fracture increases for larger grain sizes [8].

Several mechanisms have been suggested to account for the observed behavior of polycrystalline NiAl. Schulson and Barker have shown that a critical grain size exists, below which significant inelastic offset may occur [28]. The primary effect of a smaller grain size is to allow stable microcracking to occur, so that plastic flow may continue in grains favorably oriented for glide. In all grain sizes, brittle failure eventually occurs by intergranular separation and the rapid propagation of microcracks. For the non-stoichiometric Ni-49% Al (atomic) alloy, the critical grain size is ~20 μm at 400 °C and is expected to be smaller than this value for RT deformation. In nominal agreement with this prediction, ductility is observed at RT for NiAl with a grain size of 11-16 μm [24] and 2-3 μm [22]. In contrast to this prediction, however, the results of George and Liu show tensile ductility at RT with a grain size of 30 μm [29]. In fact, stable microcracks are reported to be absent altogether in the specimens exhibiting tensile ductility at RT by Hahn and Vedula, as mentioned previously. Therefore, although stable microcracking may allow plastic deformation to occur in fine-grained NiAl, this is not a general effect, and other variables may also be important.

18

It has recently been proposed that deformation-induced texture may be an important factor in achieving RT tensile plasticity [30]. These authors show that a strong <111> fiber texture is produced after extrusion of a cast Ni-45% Al alloy, and after extrusion of pre-alloyed powder of the same composition. Extruded material was used in each of the investigations reporting RT ductility for polycrystalline NiAl [22-24,29], although this process did not guarantee RT plasticity [21,27]. Electron microscopy has not yet been conducted to determine if the observed texture plays a significant role in the deformation of the samples exhibiting RT ductility. Environmental embrittlement has been documented in Fe-rich FeAl [31], but this is not expected to influence the deformation of NiAl, since most of the investigations reporting tensile ductility at RT were conducted in air [22,24,29]. Finally, it has been shown that the stress-assisted diffusional climb of dislocations may play a role in the deformation of cube-oriented single crystals [18,19], and it has been suggested that this may account for the ductility observed in polycrystalline NiAl [7]. This will be considered in detail in the following chapter.

It has often been speculated that the operation of non-<100> slip vectors may occur in polycrystalline NiAl, therefore affording some plasticity [5,8,23]. In most cases, observations of <110> and <111> dislocations have been made on single crystal samples, and these dislocations were typically short and straight, and occurred only at nodes, such that their occurrence could adequately be explained by the elastically stable interaction between appropriate mobile <100> dislocations [2,18,19,32]. Electron microscopy studies of extruded polycrystalline NiAl, where the stress, strain, strain rate, and deformation temperature were unknown and uncontrolled, has shown that <100> dislocations dominate, but short segments of <110> dislocations exist in networks and tangles and <111> dislocations were not observed [33,34]. It was therefore concluded that the <110> dislocations were not important in the deformation processes during extrusion. In both of these studies, however, the extrusions were slowly cooled in sand, and it is not clear that the dislocations observed represent the deformation mechanisms which operated during the

extrusion process. Lloyd and Loretto also examined the deformed microstructure of extruded NiAl and, in agreement with the results just cited, the majority of the dislocations were of the <100> type [5]. However, the observation of long, curved <110> dislocations, three-fold <110> dislocation nodes, and <111> dislocations led these authors to conclude that non-<100> dislocations were important in the deformation during the extrusion process. Details of the extrusion process, including extrusion temperature and cooling rate, were not reported. Non-<100> dislocations exhibiting a morphology consistent with glide have been observed in polycrystalline NiAl deformed under controlled conditions in only one case [35]. Lasalmonie claims that the activation of <110> dislocations becomes easy for stoichiometric NiAl in the temperature range of 580-680 °C, and shows a micrograph of three-fold <110> dislocation nodes. Complete details of the dislocation analysis were not provided.

In spite of the large number of investigations cited, a careful analysis of the deformation microstructure in polycrystalline stoichiometric NiAl deformed at typical strain rates (10^{-2} to 10^{-4}/sec) has not yet appeared in the literature. This information is central to the determination of the mechanism responsible for the ductility of polycrystalline NiAl, and this is clearly an area for future research. Nonetheless, it has often been assumed that the primary slip system in polycrystalline NiAl is the same as the preferred slip system in "soft" single crystals, and the data available supports this assumption. It has been shown that only three independent modes of deformation are afforded by the glide of <100> dislocations in a cubic material regardless of the number of slip planes which may operate and whether or not the dislocations cross slip [12], yet five independent modes of deformation are required to explain the ductility observed in polycrystalline NiAl above 400 °C [36]. Additional modes of deformation, such as twinning, have not been observed in polycrystalline NiAl.

2.2.3 Summary

It is clear from the discussion above that $<100>\{110\}$ and $<100>\{100\}$ are the primary slip systems in "soft" single crystals. $<111>\{110\}$ and $<111>\{112\}$ have been shown to operate in "hard" crystals from -196 °C to 300 °C, and these slip systems compete with kinking during compressive deformation. The deformation mechanism above 300 °C has not yet been established for cube-oriented single crystals. A detailed characterization of the deformation microstructure of polycrystalline NiAl deformed under controlled conditions has not yet appeared in the literature, and a careful analysis of the mode of deformation in polycrystalline NiAl which exhibits plasticity at both RT and the ductile-to-brittle transition is particularly lacking. Five independent modes of deformation are required to support ductility in a polycrystalline material, yet only three are provided by the preferred $<100>$ slip vector in NiAl. Non-$<100>$ dislocations clearly operate in single crystals, although a much higher stress is required to activate these slip modes. Limited evidence suggests that the glide of non-$<100>$ dislocations may provide the additional independent slip modes required for ductility in polycrystalline NiAl, but more convincing verification is required. The stress-assisted diffusional climb of $<100>$ dislocations has also been suggested to provide the additional modes of deformation required for polycrystalline ductility, and this proposal is considered in detail in the next chapter. Also, a new proposal based on the local activation of non-$<100>$ dislocations is developed.

CHAPTER III

THEORY

3.1 Stress-Assisted Diffusional Climb

The possibility that the stress-assisted diffusional climb of <100> dislocations may provide additional independent deformation modes, and therefore account for the ductility of polycrystals and cube-oriented single crystals of NiAl has been suggested in the literature [7,18,19]. Groves and Kelly have shown theoretically that a combination of <100> glide and the climb of <100> edge dislocations can account for the general deformation of a polycrystalline aggregate of NiAl [37]. A number of experimental observations which support this theory for the uniform deformation of cube-oriented single crystals have been discussed by Fraser and coworkers [18,19]. A critical analysis of this theory as it applies to the deformation of NiAl single crystals and polycrystals is considered in detail below, using more recent data not available at the time of Fraser's original treatment [38].

An experimental observation used to support the proposed climb of <100> dislocations was the absence of clear surface slip markings on cube-oriented compression samples, since climb of these dislocations would produce no visible slip traces [18,19]. Loretto and Wasilewski also report that surface slip markings are "very indefinite" on <100> crystals compressed at RT, but these authors clearly show that glide of <111> dislocations is responsible for the plastic strain. Wasilewski et al. report that "hard" crystals tested in tension form multiple necked regions prior to fracture, and concluded that the absence of well-defined slip traces was due to the high rate of work-hardening ($d\sigma/d\varepsilon$) measured for these crystals. A very low value of n=0.06 for the strain-hardening

22

exponent, from the relation $\sigma = K\varepsilon^n$, was given for specimens tested at 700 °C. In agreement with these observations, Pascoe and Newey [8] report a value for n of 0.05 at RT. High values of $d\sigma/d\varepsilon$ and low values for the strain-hardening exponent each indicate that a very high rate of work-hardening exists in NiAl, and the absence of well-defined slip traces on cube-oriented single crystals may therefore alternately be explained by the associated rapid delocalization, or dispersal, of slip.

The principle argument presented by Fraser et al. in support of the stress-assisted diffusional climb of <100> dislocations in "hard" crystals is based on a calculation of the magnitude to which the climb of dislocations may account for the strain rates imposed during deformation. When diffusion occurs predominantly through the bulk, and dislocations are the principal sources and sinks of vacancies, the strain rate dependence is given as [39]

$$\dot{\varepsilon} = \frac{D|b|P^3/\pi kTG^2}{\ln(4G/\pi P)} \tag{3}$$

where D is the bulk diffusion coefficient, $|b|$ is the magnitude of the Burgers vector b, P is the applied stress, k is Boltzmann's constant, T is the absolute temperature, and G is the shear modulus. Using diffusion data for Co in NiAl [40] and an estimate of the diffusion coefficient based on the enthalpy of formation of vacancies in NiAl [41], Fraser et al. calculate the strain rate due to climb to fall in a range from 10^{-4} to 10^{-6}/sec at 600 °C, in close agreement with the imposed strain rate of 10^{-4}/sec. The strain rate from Eqn. (3) at 600 °C due to the climb of <100> dislocations using a value of $D = 1.87 \times 10^{-22}$ m²/sec from the more recent diffusion data of Hancock and McDonnell [42], a shear modulus of 31.9 GPa from Rusovic and Warlimont [43], a value of 0.288 nm for the <100> Burgers vector, and an applied stress of 190 MPa (the average flow stress for "hard" crystals at 600 °C from Fig. 3) is calculated to be 5×10^{-8}/sec. If it is assumed that diffusion occurs primarily along the dislocation cores, then the predicted strain rate is given by [39]

$$\dot{\varepsilon}_c = \frac{4D_c b |P^5}{(\pi G)^4 kT}$$

(4)

where D_c is the diffusion rate along the dislocation cores. Assuming that the activation energy for diffusion along dislocation cores is one half the activation energy given for bulk diffusion in Hancock and McDonnell, a value of 2.89×10^{-13} m^2/sec is obtained for D_c, and the strain rate calculated from Eqn. (4) is 7×10^{-5}/sec. Darolia et al. record over 20% uniform elongation for "hard" single crystals tested in tension at 427 °C using a nominal strain rate of 2.3×10^{-3}/sec. Using 889 MPa as the flow stress at this temperature, strain rates of 1×10^{-10}/sec and 1×10^{-3}/sec are calculated for $\dot{\varepsilon}$ and $\dot{\varepsilon}_c$, respectively, from the equations above. It is clear from these calculations that bulk diffusion is too slow to allow <100> dislocations to climb at a sufficient rate to account for the applied strain rate. However, if mass transport occurs primarily along the dislocation cores, the calculated strain rates are of the proper order of magnitude to explain the uniform deformation of <100> single crystals.

It is important to note that the calculated strain rates are strongly dependent on the applied stress, and a similar calculation using a value of 130 MPa for the flow stress in polycrystalline NiAl at 400 °C yields a value of 2×10^{-8}/sec for $\dot{\varepsilon}_c$. At 600 °C the yield stress drops to 110 MPa, and the calculated strain rate $\dot{\varepsilon}_c$ increases to only 4×10^{-6}/sec. Each of these strain rates are too low to account for a significant fraction of the imposed strain rate in the mechanical tests on polycrystalline NiAl at the DBTT.

The calculations above must be approached with extreme caution, since a large extrapolation of the diffusion data is required, and this extrapolation assumes that the activation energy for diffusion remains constant. In polycrystalline material, this is clearly a point of concern, since the activation energy for diffusion generally changes as the primary mechanism of mass transport changes from bulk diffusion to "short-circuit" diffusion along grain boundaries or dislocation cores. To a first order-approximation, this has been accounted for in the calculations of $\dot{\varepsilon}_c$ above. However, it has been shown that

24

the activation energy for self-diffusion through the bulk decreases as the temperature is decreased in a vacancy migration simulation for diffusion in an ordered CsCl lattice [44]. This prediction fits the behavior noted for the B2 compounds CuZn [45] and AuCd [46]. In fact, although Hancock and McDonnell interpret their data in terms of the standard Arrhenius equation, they note that some curvature of the log(D) vs. 1/T plot is possible for NiAl. A decrease in the activation energy of diffusion at lower temperatures would tend to increase the diffusion coefficient at these temperatures, thereby increasing the strain rate that may be supported by climb.

In addition to the experimental observations already discussed, several points remain which cannot be rationalized in terms of the proposed climb mechanism, particularly concerning the application of this model to the deformation of polycrystalline NiAl. The first observation is that tensile ductility is reported to occur in polycrystalline NiAl at RT [22,24,29], where the strain rate that could be supported by climb is many orders of magnitude lower than the rates calculated above. However, the effect of a strongly textured microstructure has not been adequately addressed, and this texture may relax the requirements of compatibility at grain boundaries, so that glide of <100> dislocations alone may account for the ductility observed at RT. The second observation that is difficult to reconcile with the climb model is that NiAl can be extruded at temperatures as low as 550 °C without cracking or forming internal voids [33,34]. Although some adiabatic heating certainly occurs, climb is not expected to contribute significantly at the high strain rates typically employed during extrusion (10^0/sec to 10^1/sec). Finally, strain rate change tests can yield information regarding the operative deformation mechanism. From the relation $\dot{\epsilon}=K\sigma^m$, a plot of log($\dot{\epsilon}$) vs. log(σ) is expected to exhibit a slope of 3 to 5 if diffusion-controlled processes, such as climb, are operative (see, for example, Eqn. (3)) [39,47,48], and a slope of 5 to 10 if glide is the operative mechanism [49]. Data from several authors [18,50,51] strongly suggests that glide of dislocations is the dominant mechanism below about 1000 °C (Fig. 6). Fraser et al. argue that change of strain rate

25
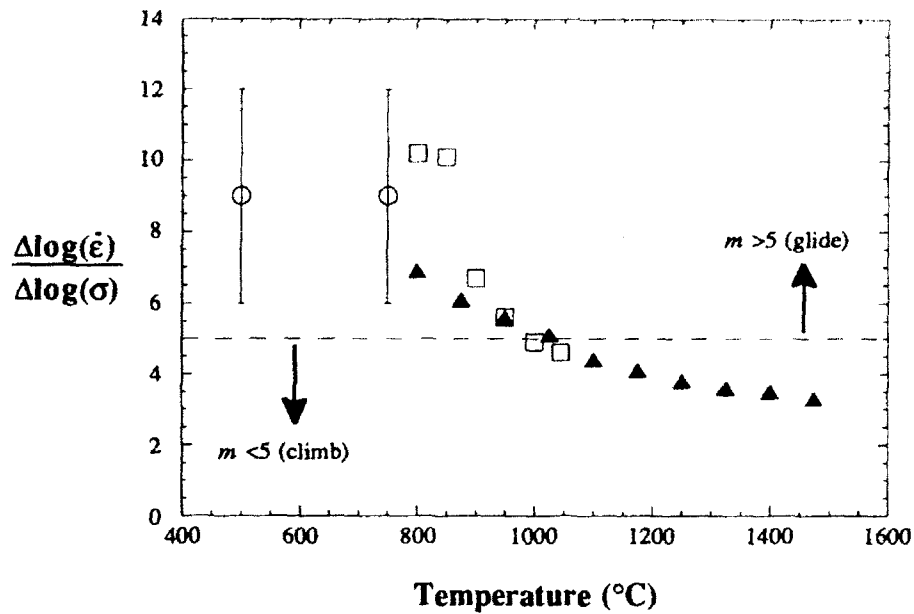
Figure 6. Strain rate hardening exponent *m* as a function of temperature from (○) Fraser et al. [18], (▲) Vandervoort et al. [50], and (□) Yang and Dodd [51]. An exponent of 3 to 5 indicates deformation by diffusion controlled processes, and an exponent of 5 to 10 is typical for glide in bcc materials.
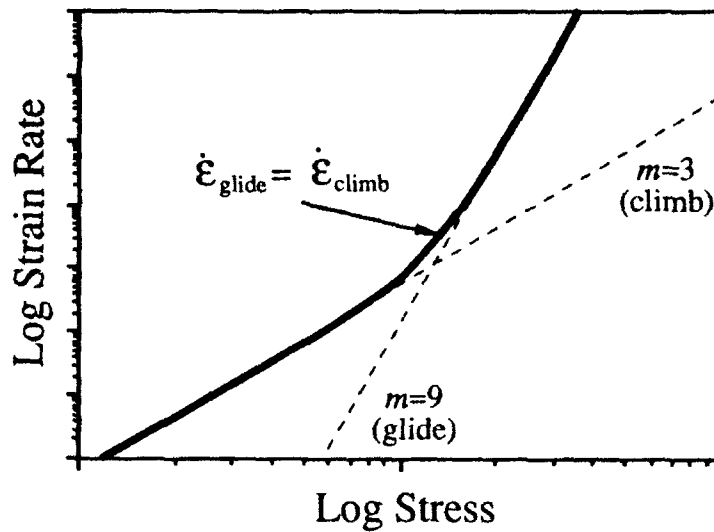
Figure 7. Schematic plot of log strain rate vs. log stress illustrating the transition from glide-controlled deformation to climb-controlled creep.

tests may be deceptive, since an increase in the imposed strain rate will be accommodated primarily by glide if the original strain rate is accommodated equally by climb and glide, as illustrated in Fig. 7. However, using this same argument, an exponent representative of climb is expected for a decrease in the imposed strain rate from the condition of equal climb and glide. This balance between climb and glide is expected to be met only under limited conditions of temperature and strain rate. The data cited in Fig. 6 represent tests covering a wide range of strain rates and temperatures, and the results consistently indicate that glide is the primary mechanism of deformation below 1000 °C.

It is apparent from the discussion above that the mechanism by which polycrystalline NiAl is able to deform plastically is not understood. Climb seems an unlikely mechanism at the ductile-to-brittle transition temperature, although the effect of a possible decrease in the activation energy with decreasing temperature and of potentially rapid mass transport associated with short-circuit diffusion has not been adequately addressed. Each of the observations discussed above support the proposal that glide alone is responsible for deformation in NiAl. Since <100> dislocations provide only three independent strains, dislocations with non-<100> Burgers vectors are required if glide alone is to satisfy the von Mises criterion in NiAl. <111> dislocations have clearly been established to operate in NiAl, but these dislocations are proposed to contribute to plasticity only in cube-oriented single crystals tested below 300 °C [4,10,13]. Only limited evidence is available for the activation of <110> dislocations [5,35], and these dislocations are observed in single crystals only when the samples are deformed in creep [52,53]. A plausible mechanism for the activation of non-<100> dislocations in polycrystalline NiAl has not appeared in the literature. One such mechanism, the activation of non-<100> dislocations at local stress concentrations, is outlined below.

3.2 Local Activation of Non-<100> Dislocations

Constraints at grain boundaries and interphase boundaries have been shown to play an important role in the activation of slip systems. An analysis of the elastic and plastic incompatibility in bicrystals of Al [54] and Fe-3% Si [55] has been shown to account for the unexpected slip systems observed to operate locally at the grain boundary. Noebe and Gibala have shown that a thin oxide coating on single crystals of NiAl reduces the flow stress by as much as 60%, and argue that elastic and plastic constraints at the NiAl/oxide interface are responsible for this reduction [56]. Severe localized deformation at grain boundaries in polycrystalline NiAl has been observed [7,25], and Rozner and Wasilewski have speculated that <111> dislocations may operate in these regions. The possibility that elastic and plastic incompatibility at grain boundaries may account for the activation of non-<100> dislocations is discussed below.

Consider the deformation of a single grain favorably oriented for primary <100>{110} slip in polycrystalline NiAl. Sources within the grain will generate dislocations, which will glide until an obstacle, such as a grain boundary, is encountered. A local grain boundary stress will result from the pile-up of dislocations and, generally speaking, this stress will increase with increasing deformation in the first grain until some critical event occurs, including deactivation of the dislocation source due to an increasing back stress, the initiation of fracture, or the nucleation of dislocations in the adjacent grain. It is certainly conceivable that the adjoining grain may not be favorably oriented for the nucleation of <100> slip, and a very large, triaxial state of stress may accumulate at the grain boundary. Even if <100> dislocations are activated in the neighboring grain, a residual stress resulting from plastic incompatibility at the boundary may arise if the grains are oriented such that additional degrees of freedom beyond the three afforded by <100> slip are required. In each case, a concentrated stress field remains which may be capable of nucleating non-<100> dislocations required for plastic compatibility.

The important question to ask is whether <110> or <111> dislocations can be activated in such a situation, since both the energy to create these dislocations and the stress required to move them are significantly higher than the energy and stress required to produce <100> slip. As mentioned in Chapter II, a careful TEM investigation of the deformation microstructure in polycrystalline NiAl after controlled deformation has not yet appeared in the literature, so direct evidence of the local activation of non-<100> dislocations is not available. Pertinent questions remain in those experiments where non-<100> dislocations have been reported, since it is not clear whether the dislocations observed were responsible for accommodating the imposed deformation, or whether they formed as the sessile reaction products of mobile <100> dislocations. Additional difficulties may arise, such as those arising from small sampling volumes, since the volume of material available for investigation in a typical TEM study is very limited, and activation of non-<100> dislocations may occur in only a fraction of the grains. An experiment where the state of stress is both known and controlled is required to effectively study the activation of non-<100> slip at grain boundaries. It is therefore proposed to investigate this possibility by modeling the state of stress at grain boundaries in NiAl, and to verify experimentally the predictions of this model in oriented NiAl bicrystal compression specimens. In the next section, a model to calculate the stress tensor at a grain boundary in NiAl is developed, and the results of the calculations are presented.

3.2.1 Determination of Bicrystal Orientations

A continuum approach was used to calculate the stress tensor which results from elastic and plastic incompatibility at an NiAl grain boundary. The calculations represent a first-order approximation for the stress tensor at the grain boundary, and the primary role of the calculations was to provide guidance in the selection of bicrystal orientations for subsequent experimentation. A specific mechanism for slip transmittal at the grain boundary is neither assumed nor proposed by the calculation. No attempt was made to

determine the statistical relevance of the results obtained for specific bicrystals as it may apply to the plasticity of a polycrystalline aggregate of randomly oriented grains. Practical considerations concerning the preparation and testing of suitable specimens have influenced the configuration modeled.

Consider a bicrystal consisting of orientations A and B, separated by a planar interface perpendicular to the compression axis (Fig. 8). One of the crystals is oriented for easy single slip on one of the primary <001>{110} slip systems (crystal B), and the other crystal is oriented so that primary slip is initially unfavored. An external displacement is applied to the bicrystal until $\tau_{crss}^{<100>}$ is exceeded in crystal B, and the resulting stress tensor at the grain boundary is calculated by summing the contributions from the directly applied stress, the stress resulting from the elastic incompatibility of the two crystals, and the plastic incompatibility stress arising from plastic deformation in crystal B. Once the stress at the grain boundary is calculated, it can be resolved onto any slip system of interest in crystal A. The purpose of these calculations is to determine if bicrystal orientations exist where $\tau_{crss}^{<111>}$ is exceeded on <111> slip systems in crystal A before $\tau_{crss}^{<100>}$ is achieved on <001> slip systems in that crystal.

In order to perform the calculations, a "grain boundary" coordinate system common to both crystals is defined, such that the compression axis is x_3' and is normal to the grain boundary, and both x_1' and x_2' lie in the plane of the grain boundary and form a right-handed orthogonal coordinate system. The primed notation is used to indicate reference to this grain boundary coordinate system. Transformations are performed on the primary slip plane and slip direction in crystal B, on the elastic compliance and stiffness tensors for crystals A and B, and on the slip systems of interest in crystal A.

The first step in calculating the stress at the grain boundary is to calculate the resolved shear stress on the potential slip systems in crystal A resulting from the stress directly applied to the bicrystal. Assuming that NiAl follows Schmid's law, the applied stress is given by the relation

30
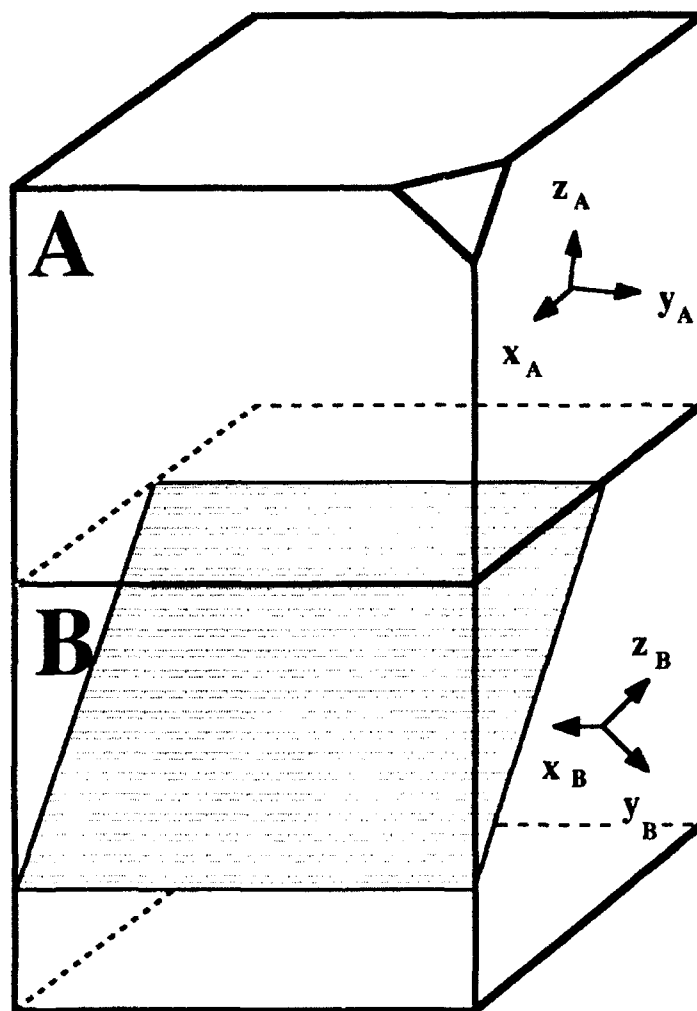
Figure 8.   The bicrystal geometry modeled and tested, showing the different crystal axes of crystal A and crystal B. The slip plane in crystal B is shown schematically.

31

$$\sigma_A = \sigma_B = \tau_{crss}^{<100>}/\Phi_B \tag{5}$$

where Φ_B is the Schmid factor for the active primary slip system in crystal B. The resolved shear stress on each of the slip systems in crystal A due to the directly applied load is then calculated from

$$\tau_A^{appl}(p) = (\sigma_A)\Phi_p \tag{6}$$

where Φ_p is the Schmid factor for the pth slip system in crystal A.

The second contribution to the grain boundary stress tensor is from the elastic incompatibility of the two crystals. If the two grains are considered to be decoupled, the elastic strain in each crystal is obtained from the generalized form of Hooke's Law as

$$\epsilon'_A(i,j)_{elas} = [S'_A(i,j,k,l)]\sigma'(k,l) \tag{7a}$$

$$\epsilon'_B(i,j)_{elas} = [S'_B(i,j,k,l)]\sigma'(k,l) \tag{7b}$$

where $S'(i,j,k,l)$ is the transformed compliance matrix, and summation over the repeated indices is assumed. Since the bicrystal is subjected to uniaxial compression, and since only very small strains are considered so that work-hardening may be neglected, $\sigma'(3,3) = \sigma_A$, and all other $\sigma'(k,l) = 0$, so that the two relations above become

$$\epsilon'_A(i,j)_{elas} = [S'_A(i,j,3,3)]\sigma_A \tag{8a}$$

$$\epsilon'_B(i,j)_{elas} = [S'_B(i,j,3,3)]\sigma_A \tag{8b}$$

If we now couple the two crystals, an elastic strain must be applied to each crystal so that compatibility is achieved at the grain boundary. In general, this compatibility strain will be different for each crystal since the partitioning of the strain depends on the orientation of each crystal. The problem is simplified here by assuming that the strain is divided equally between the two crystals, so that

$$\Delta\epsilon'_A(i,j)_{elas} = 1/2[\epsilon'_B(i,j)_{elas} - \epsilon'_A(i,j)_{elas}] \tag{9}$$

Since a difference in elastic strains normal to the grain boundary will result in no stresses for the specimen configuration described above, $\Delta\epsilon'_A(3,3)$ is set to zero. The stress that will be required to bring crystal A to compatibility at the grain boundary is calculated from this elastic incompatibility strain as

$$\Delta\sigma'_A(k,l)_{elas} = [C'_A(k,l,i,j)](\Delta\epsilon'_A(i,j)_{elas}) \tag{10}$$

where $C'_A(k,l,i,j)$ is the transformed stiffness matrix for crystal A. Finally, this stress must be resolved onto each slip system of interest in crystal A. To accomplish this transformation, each slip system is considered to form a new coordinate system, where the slip plane normal defines the new x_3 axis and the Burgers vector is parallel to the new x_1 axis. The stress $\Delta\sigma'_A(k,l)_{elas}$ is transformed to $\sigma_A^{elas}(k,l)_p$ for each of these slip systems. When the stress is transformed as specified above, the resolved shear stress on each slip system due to elastic incompatibility is given by

$$\tau_A^{elas}(p) = \sigma_A^{elas}(3,1)_p \tag{11}$$

The final contribution to the stress at the grain boundary is the stress that results from plastic incompatibility. This is modeled by considering the imposed plastic strain to be a homogeneous strain distributed evenly throughout crystal B. For a simple shear in crystal B of magnitude $\tan\phi$, the plastic strain matrix is given by

$$\epsilon'_B(i,j)_{plas} = (\phi/2)[(n'_B(i))(b'_B(j)) + (n'_B(j))(b'_B(i))] \quad [57] \tag{12}$$

where $n'_B(i)$ and $b'_B(i)$ are the components of the slip plane normal and the Burgers vector in crystal B in terms of the grain boundary coordinate system, respectively. For a given imposed normal plastic strain, the value of ϕ may be determined, since $\epsilon'_B(3,3)_{plas}$, $n'_B(3)$, and $b'_B(3)$ are known. Note that the homogeneous strain experienced by crystal B is approximately twice the macroscopic strain imposed on the bicrystal, since all of the plastic deformation initially occurs in crystal B alone. Therefore,

$$\phi = 2\epsilon'_B(3,3)_{plas}/[(n'_B(3))(b'_B(3))] \tag{13}$$

Once ϕ is known, then all nine terms of the plastic strain $\epsilon'_B(i,j)_{plas}$ can be calculated. This plastic strain in crystal B is accommodated elastically in crystal A, until either the fracture stress is exceeded, or until a stress sufficient to activate slip in crystal A is achieved. The difference in plastic strain across the grain boundary is given by

$$\Delta\epsilon'_A(i,j)_{plas} = [\epsilon'_B(i,j)_{plas} - \epsilon'_A(i,j)_{plas}] = \epsilon'_B(i,j)_{plas} \tag{14}$$

This compatibility strain is not partitioned between crystals A and B as was done for the

33

elastic incompatibility strain, and is rationalized by noting that the plastic incompatibility strain is a direct result of the presence of a given amount of plastic deformation in crystal B. If this strain is not accommodated fully in crystal A, then some fraction must be accommodated, either elastically or plastically, in crystal B. Crystal B cannot accommodate an additional elastic strain since it is already loaded beyond its elastic limit by definition. The possibility that a small amount of the plastic incompatibility strain is accommodated in crystal B at the grain boundary by producing slip on systems other than the initially active slip system, therefore setting up a strain gradient in crystal B, is not considered here. The stress required to enforce compatibility in crystal A at the grain boundary is therefore given as

$$\Delta\sigma'_A(k,l)_{plas} = [C'_A(k,l,i,j)](\Delta\epsilon'_A(i,j)_{plas}) \qquad (15)$$

This stress is resolved onto the slip systems of interest in crystal A using the transformation to the slip system coordinate systems defined above for the elastic incompatibility stress. Therefore,

$$\tau_A^{plas}(p) = \sigma_A^{plas}(3,1)_p \qquad (16)$$

It must be emphasized that a homogeneous plastic strain is assumed in the calculation of τ_A^{plas}. However, intense dislocation activity in NiAl is often observed in bands about 1 μm thick, and these bands are separated by large volumes of dislocation-free material [13]. Therefore, plastic strains significantly larger than the macroscopic homogeneous plastic strain may occur locally, and the plastic incompatibility stresses calculated assuming a homogeneous distribution of strain should be considered as a lower bound of the stress that may arise from plastic deformation. A factor to account for this concentration of plastic strain may be inserted into the calculations, but would be subjective in nature, since an experimental basis for choosing a specific, or even representative, concentration factor does not exist. The localized nature of the slip bands is acknowledged implicitly by not setting $\Delta\epsilon'_A(3,3)_{plas} = 0$. If the plastic strain were purely homogeneous, then no stress would result from a difference in normal strain perpendicular to the grain

34

boundary, as in the case for the elastic incompatibility. However, since the strain tensor within the slip band is surrounded by material where $\varepsilon'_B(i,j)_{plas} = 0$, all strain components, including $\Delta\varepsilon'_A(3,3)_{plas}$, will result in an incompatibility stress.

The total resolved shear stress on each of the slip systems in crystal A is obtained by summing the contributions from the directly applied stress (Eqn. (6)), the elastic incompatibility stress of the two crystals (Eqn. (11)), and the plastic incompatibility stress (Eqn. (16)), as shown below

$$\tau_A^{tot}(p) = [\tau_A^{appl}(p) + \tau_A^{elas}(p) + \tau_A^{plas}(p)] \qquad (17)$$

Calculations of the stress at the interface have been carried out for an applied normal strain ranging from 0.3% to 1.5%. Simulations have been performed at RT and 660 °C. Data for the elastic constants at these temperatures were obtained from Rusovic and Warlimont [43], and values for $\tau_{crss}^{<100>}$ and $\tau_{crss}^{<111>}$ as a function of temperature were taken from Fig. 2(b). A value of 534 MPa for $\tau_{crss}^{<111>}$ at 660 °C was obtained by extrapolating from the data of Bowman et al. in Fig. 2(b).

Six compression axes for crystal B were chosen from on or near the great circle of a stereographic projection connecting the [111] and the [010] poles, and eight orientations for the compression axis of crystal A were chosen within about 25° of the [001] axis. Each of the axes in crystal B provide for single slip on the [010](101) slip system. The bicrystal axes for crystal B are listed in Table 1 along with the compression axes for crystal A which result in promising bicrystal orientations. Other crystal A axes considered were $[126]_A$, $[216]_A$, $[113]_A$, and $[012]_A$. Twenty-four vectors perpendicular to each compression axis in crystal A were identified as x_1 axes, and eight vectors for were selected as x_1 for each compression axis in crystal B. These vectors provided for rotation about the compression axes in crystals A and B.

Several bicrystal orientations were identified where the critical resolved shear stress for the glide of <111> dislocations at RT was exceeded on slip systems with a <111> vector before reaching the critical resolved shear stress for the glide of <100> dislocations

35

Table 1   Preliminary bicrystal orientations identified.

Crystal B Compression Axes	Crystal A Compression Axes	
	RT	660 °C
[232]$_B$	[001]$_A$	[001]$_A$
[353]$_B$		
[121]$_B$	[016]$_A$	[016]$_A$
[131]$_B$		[013]$_A$
[141]$_B$		
[231]$_B$	[116]$_A$	[116]$_A$

on slip systems with a <100> slip vector. Four promising families of bicrystals are listed in Table 1 by indicating the compression axes in crystals A and B which result in a prediction of <111> slip. Several of these successful bicrystals resulted for each of the four pair of compression axes given in Table 1. In each case, except for the $[116]_A \parallel [231]_B$ orientation, a successful bicrystal resulted when the $[100]_A$ axis was aligned with the $[\bar{1}01]_B$ axis. These vectors were therefore taken as the x_1 axes for crystal A and crystal B, respectively.

CHAPTER IV

EXPERIMENTAL APPROACH

Two bicrystal orientations were selected based on the calculations described in

Chapter III. The first bicrystal was chosen to maximize the possibility of observing <111>

slip in crystal A. A bicrystal was selected in which the activation of <111> dislocations

was predicted to occur at RT in crystal A and the resolved shear stress on the most highly

stressed <100>{110} slip system in crystal A was as low as possible. The bicrystal that

satisfied these requirements is the bicrystal where $[001]_A \parallel [232]_B$ and $[100]_A \parallel [\bar{1}01]_B$.

This is designated as the [232] bicrystal. and a superimposed set of stereographic

projections for this bicrystal is given in Fig. 9. Results from the calculations for the [232]

bicrystal are given in Table 2. A second bicrystal was chosen to investigate an bicrystal

orientation where <111> slip was not predicted to occur. The bicrystal described by

$[001]_A \parallel [353]_B$ and $[100]_A \parallel [\bar{1}01]_B$, hereafter referred to as the [353] bicrystal, was

chosen, since <111> slip was not predicted to occur in crystal A at RT, yet this bicrystal is

similar to the [232] bicrystal in that a rotation of only 3° exists between the [232] axis and

the [353] axis. Fig. 10 shows a superimposed set of stereographic projections for this

bicrystal, and results of the calculations are provided in Table 3. In these two bicrystals,

the compression axis (and the grain boundary normal) is parallel to the $[232]_B$ and $[353]_B$

vectors, respectively. Compression tests were performed on these bicrystals at RT and

660 °C, and the active slip planes were determined by two-surface slip trace analysis. The

deformed microstructure was characterized by TEM, and g·b contrast analyses [58]were

performed to determine the Burgers vector of the dislocations. The observations were

38

Figure 9 Superimposed stereographic projection for the [232] bicrystal.

Table 2. The resolved shear stress $\tau_A^{tot}(p)$ (in MPa) for the $[001]_A \parallel [232]_B$ bicrystal. At RT, $\tau_{crss}^{<111>}=571$ MPa and $\tau_{crss}^{<100>}=75$ MPa, and at 660 °C $\tau_{crss}^{<111>}=534$ MPa and $\tau_{crss}^{<100>}=55$ MPa . The predicted slip systems are indicated by an asterisk.

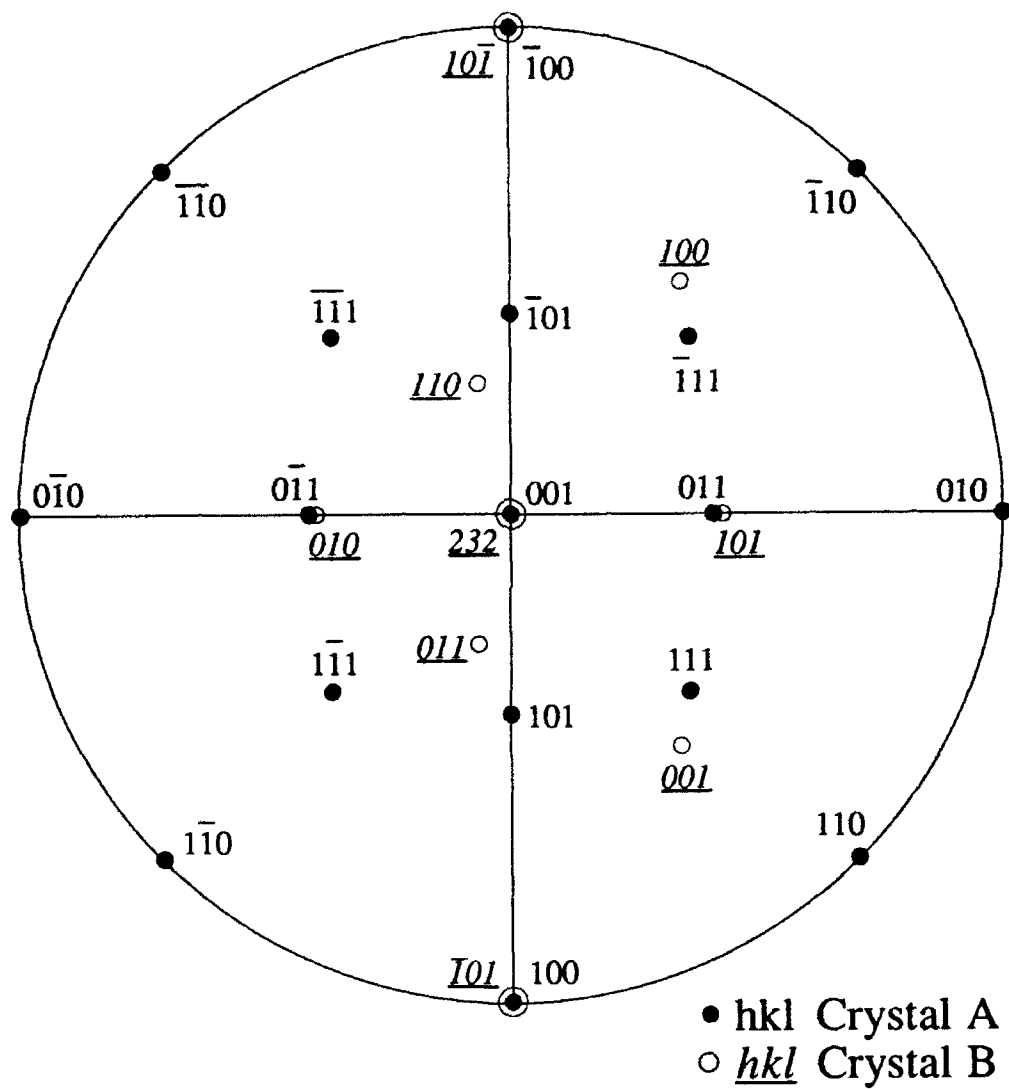| SLIP SYSTEM	RT			660 °C		
	ε=0.6%	ε=0.9%	ε=1.2%	ε=0.6%	ε=0.9%	ε=1.2%
[11Ī](112)	-301	-412	-523	-257	-361	-464
[1Ī1](Ī12)	301	412	523	257	361	464
[Ī11](1Ī2)	312	430	547	268	377	486
[111](11Ī)	-312	-430	-547	-268	-377	-486
[1Ī1](121)	271	389	507	242	351	461
[11Ī](Ī21)	-271	-389	-507	-242	-351	-461
[111](1Ī1)	261	372	483	232	335	439
[Ī11](12Ī)	-261	-372	-483	-232	-335	-439
[Ī11](211)	51	58	65	36	42	48
[111](Ī11)	51	58	65	36	42	48
[11Ī](2Ī1)	-30	-23	-16	-15	-10	-4
[1Ī1](21Ī)	-30	-23	-16	-15	-10	-4
[Ī11](110)	-121	-181	-241	-113	-170	-226
[1Ī1](110)	139	211	284	131	197	264
[111](1Ī0)	121	181	241	113	170	226
[11Ī](1Ī0)	139	211	284	131	197	264
[Ī11](101)	209	281	353	175	242	308
[11Ī](101)	-191	-251	-311	-158	-214	-270
[111](10Ī)	-209	-281	-353	-175	-242	-308
[1Ī1](10Ī)	-191	-251	-311	-158	-214	-270
[1Ī1](011) *	331	463	595	288	411	534
[11Ī](011) *	-331	-463	-595	-288	-411	-534
[111](01Ī) *	-331	-463	-595	-288	-411	-534
[Ī11](01Ī) *	-331	-463	-595	-288	-411	-534
[1Ī0[(110)	160	240	321	149	225	300
[110](1Ī0)	160	240	321	149	225	300
[10Ī](101)	-245	-326	-407	-204	-279	-354
[101](10Ī)	-245	-326	-407	-204	-279	-354
[01Ī](011)	-405	-567	-728	-353	-504	-654
[011](01Ī)	-405	-567	-728	-353	-504	-654
[001](110)	16	26	37	15	24	33
[001](1Ī0)	-16	-26	-37	-15	-24	-33
[010](101)	16	26	37	15	24	33
[010](10Ī)	-16	-26	-37	-15	-24	-33
[100](011)	0	0	0	0	0	0
[100](01Ī)	0	0	0	0	0	0
[010](100)	0	0	0	0	0	0
[001](100)	0	0	0	0	0	0
[100](010)	0	0	0	0	0	0
[001](010)	22	37	52	22	34	46
[100](001)	0	0	0	0	0	0
[010](001)	22	37	52	22	34	46
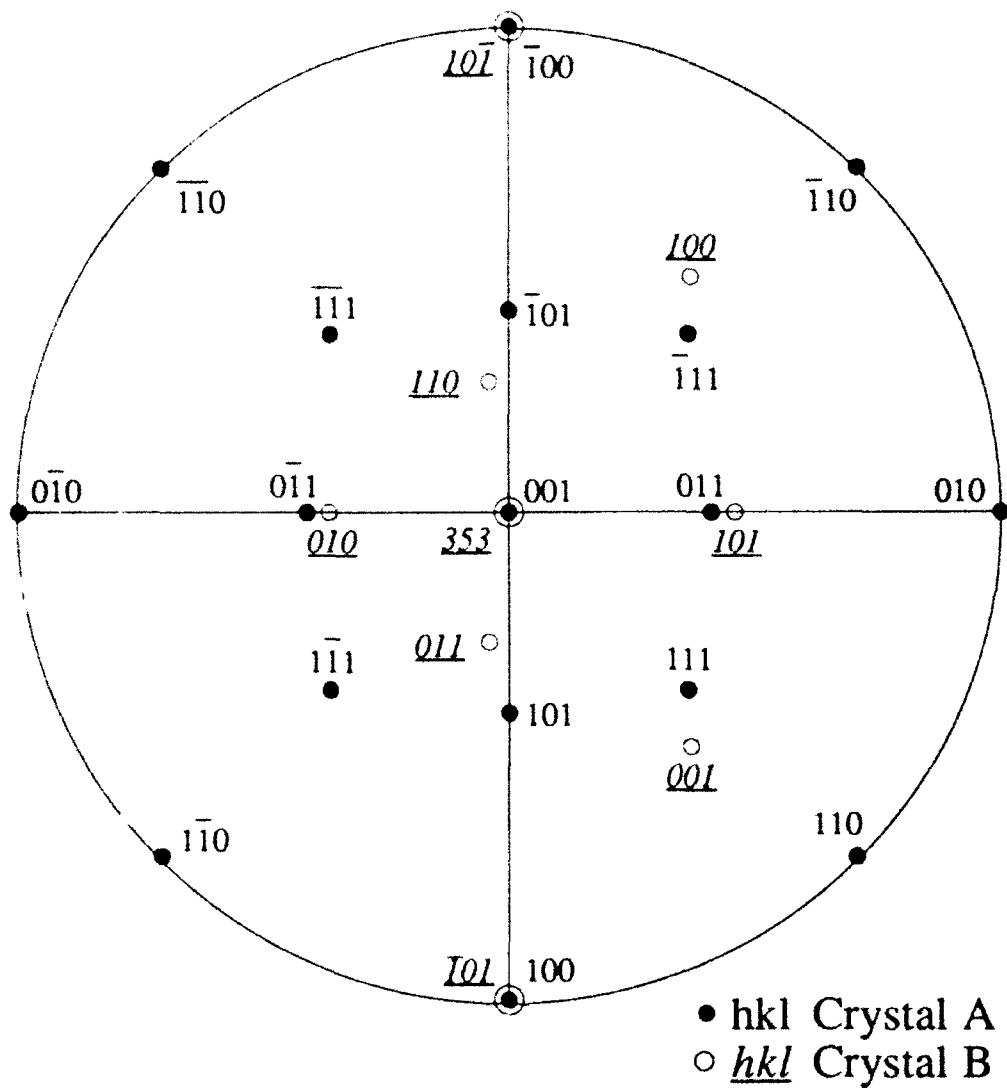
Figure 10   Superimposed stereographic projection for the {353} bicrystal.

Table 3. The resolved shear stress $\tau_A^{tot}(p)$ (in MPa) for the $[001]_A \parallel \{353\}_B$ bicrystal. At RT, $\tau_{crss}^{<111>}=571$ MPa and $\tau_{crss}^{<100>}=75$ MPa, and at 660 °C $\tau_{crss}^{<111>}=534$ MPa and $\tau_{crss}^{<100>}=55$ MPa. The predicted slip systems are indicated by an asterisk.

SLIP SYSTEM	RT			660 °C		
	$\varepsilon=0.6\%$	$\varepsilon=0.9\%$	$\varepsilon=1.2\%$	$\varepsilon=0.6\%$	$\varepsilon=0.9\%$	$\varepsilon=1.2\%$
$[11\bar{1}](112)$	-311	-426	-541	-267	-375	-483
$[1\bar{1}1](\bar{1}12)$	311	426	541	267	375	483
$[\bar{1}111](1\bar{1}2)$	349	486	622	301	427	553
$[111](11\bar{2})$	-349	-486	-622	-301	-427	-553
$[1\bar{1}1](121)$	308	444	581	275	401	527
$[11\bar{1}](\bar{1}21)$	-308	-444	-581	-275	-401	-527
$[111](1\bar{2}1)$	270	385	500	241	349	457
$[\bar{1}11](12\bar{1})$	-270	-385	-500	-241	-349	-457
$[\bar{1}11](211)$	80	101	122	60	78	96
$[111](\bar{2}11)$	80	101	122	60	78	96
$[11\bar{1}](2\bar{1}1)$	-3	19	40	8	26	44
$[1\bar{1}1](21\bar{1})$	-3	19	40	8	26	44
$[\bar{1}11](110)$	-110	-164	-218	-104	-156	-208
$[1\bar{1}1](110)$	176	267	358	163	247	330
$[111](1\bar{1}0)$	110	164	218	104	156	208
$[11\bar{1}](1\bar{1}0)$	176	267	358	163	247	330
$[\bar{1}11](101)$	248	339	430	209	292	375
$[11\bar{1}](101)$	-181	-235	-289	-150	-201	-253
$[\cdot\cdot\cdot](10\bar{1})$	-248	-339	-430	-209	-292	-375
$[1\bar{1}1](10\bar{1})$	-181	-235	-289	-150	-201	-253
$[1\bar{1}1](011)$	357	502	647	313	448	583
$[11\bar{1}](011)$	-357	-502	-647	-313	-448	-583
$[111](01\bar{1})$	-357	-502	-647	-313	-448	-583
$[\bar{1}11](01\bar{1})$	-357	-502	-647	-313	-448	-583
$[1\bar{1}0[(110)$	175	264	353	164	247	329
$[110](1\bar{1}0)$	175	264	353	164	247	329
$[10\bar{1}](101)$	-263	-351	-440	-219	-302	-385
$[101](10\bar{1})$	-263	-351	-440	-219	-302	-385
$[01\bar{1}](011)$	-438	-615	-793	-383	-549	-714
$[011](01\bar{1})$	-438	-615	-793	-383	-549	-714
$[001](110)$	58	90	122	51	78	105
$[001](1\bar{1}0)$	-58	-90	-122	-51	-78	-105
$[010](101)$	58	90	122	51	78	105
$[010](10\bar{1})$	-58	-90	-122	-51	-78	-105
$[100](011)$	0	0	0	0	0	0
$[100](01\bar{1})$	0	0	0	0	0	0
$[010](100)$	0	0	0	0	0	0
$[001](100)$	0	0	0	0	0	0
$[100](010)$	0	0	0	0	0	0
$[001](010)$ *	82	127	172	72	111	149
$[100](001)$	0	0	0	0	0	0
$[010](001)$ *	82	127	172	72	111	149

compared with he predictions of the stress model for the bicrystals tested. A detailed

description of the experimental procedures is given in Chapter V.

CHAPTER V

EXPERIMENTAL PROCEDURE

5.1 Specimen Preparation

Bicrystal compression samples were prepared by cutting single crystal slices of the desired orientation from a large single crystal of NiAl, and diffusion bonding the two slices together so that the desired relation between the crystal axes was achieved. The geometry of the bicrystal compression samples is shown schematically in Fig. 8. The interface was perpendicular to the compression axis to minimize the possibility of premature fracture at the grain boundary as a result of elastic and plastic incompatibility. The procedure for single crystal preparation, bonding, and machining is detailed below.

5.1.1 Single Crystal Preparation

A single crystal bar of NiAl measuring approximately 2.5 cm by 4 cm by 10 cm was supplied by Dr. R. Darolia of the General Electric Company. The crystal was charged to the stoichiometric composition, and was investment cast using a modified Bridgeman technique. Integrity and quality of the crystal was determined by visual inspection after annealing and thermal etching. The bulk composition was determined by gravimetric techniques, and emission spectroscopy was employed for impurity analysis. Interstitial elements were analyzed using the vacuum fusion technique.

Laue back-reflection was used to orient the single crystal bar for machining into single crystal slices. A 3 cm working distance was used, and the alignment errors were typically $\pm 1°$. The single crystal bar was attached to a modified three-axis goniometer from the South Bay Co. using epoxy glue, and after positioning the single crystal bar so that the

44

desired compression axis was aligned with the x-ray beam, slices were cut with a wire electro-discharge machine (EDM). The slices were 7.5 mm thick, and were cut from the single crystal bar in the plane parallel to the front of the goniometer base, which was perpendicular to the x-ray beam. The cut surfaces were polished through 0.05 μm alumina to remove the recast layer from the EDM process and to provide a flat, clean surface suitable for diffusion bonding. As a check, the single crystal slices were placed on a eucentric three-axis goniometer, and the crystal direction normal to the face of the single crystal slice (that is, the compression axis) was measured once again with Laue back-reflection. This normal of the slice was within 1° of the desired direction in all cases. While still mounted on the goniometer, slices for crystal A were rotated about the compression axis so that the [100] direction (x_A) was in the horizontal plane. The goniometer was then placed on a precision bench plate, and a line was scribed on one face of the crystal along the [100] direction. The same procedure was followed for crystal B slices, except that the scribe mark was made along the [$\bar{1}$01] direction (x_B). These scribe marks were to allow alignment of x_A and x_B prior to diffusion bonding.

5.1.2 Diffusion Bonding

The surfaces of the single crystal slices to be bonded (opposite the faces with the scribe marks) were lightly polished on 0.05 μm alumina to remove any contamination that may have accumulated during handling, and were then rinsed in acetone and dried. Straight-sided strips of cardboard about 12 cm long (from 3X5 cards) were taped along the scribe marks on a crystal A slice and a crystal B slice. After ensuring that the faces to be bonded were free of contamination, the surfaces were placed in contact with one another, and the slices were rotated until the two cardboard strips were judged to be parallel. The two slices were then temporarily clamped together in a small jig. Three small strips of Ni sheet were spot-welded to the single crystal slices to hold the two slices in position during handling prior to diffusion bonding. The jig and the cardboard strips were then removed.

Two techniques were used to bond the single crystal slices. The first technique used a displacement-controlled MTS machine to apply the bonding strain. The single crystal slices were placed between two tungsten platens, and graphite foil was used as a lubricant and reaction barrier. The graphite foil was pre-compressed to about 35 MPa to reduce the compliance of this layer. A cylinder of Ti sheet surrounded the slices during bonding to prevent oxygen from reaching the bicrystal. A nominal strain of 7% was imposed, and the bonding was accomplished in a vacuum of $\sim 10^{-9}$ Pa ($\sim 10^{-5}$ torr) at 1200 °C. The bonding strain was applied in the first few minutes of the bond run, and the bicrystal was then held at the bonding temperature for four hours. During this time, nearly all of the elastic strain remaining in the sample was converted to plastic strain.

In the second technique, the single crystal slices were placed between two Mo platens, which were held together by two Mo bolts (Fig. 11). As before, pre-compressed graphite foil was used. The bonding strain was imposed by the difference in thermal expansion between the Mo bolts and the NiAl slices. The thermal expansion at 1200 °C is $(\Delta l/l_0)_{NiAl}=0.019/°C$ for NiAl [59] and $(\Delta l/l_0)_{Mo}=0.007/°C$ for Mo [60]. From this, the bonding strain at 1200 °C is simply given by

$$\varepsilon = (\Delta l/l_0)_{NiAl}-(\Delta l/l_0)_{Mo} = 1.2\% \tag{18}$$

The bonding operation was carried out in a vacuum furnace at 1200 °C for four hours. The base pressure was $\sim 10^{-9}$ Pa, and a Ti getter was used as before.

One [232] and one [353] bicrystal was produced by each of the two techniques described. After bonding, the bicrystals were subjected to a vacuum anneal of 1400 °C for 8 hours.

5.1.3 Specimen Machining

Bonded bicrystal slices were machined into rectangular parallelepipeds about 5 mm on a side and ~15 mm tall using wire EDM. About ten samples were obtained from each bonded bicrystal. The aspect ratio was varied from 2.4:1 to 3:1 to control the deformation
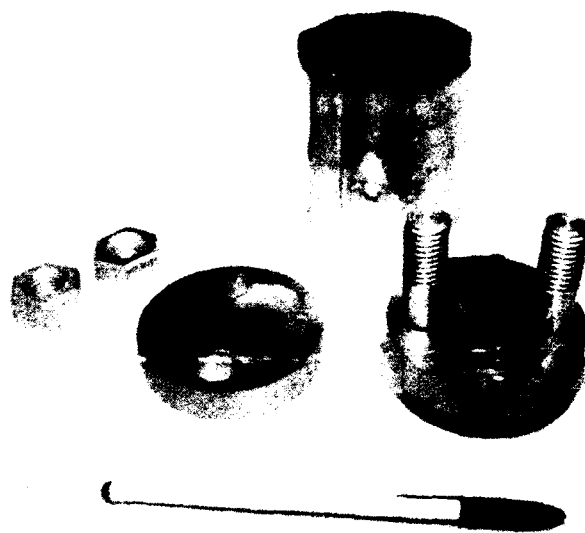
Figure 11   Mo bonding jig used to diffusion-bond NiAl single crystal slices.

in crystal B, as will be discussed later. At least 100 µm was gently ground from each of the six sides to remove the recast layer, and the four long faces were polished through 0.05 µm alumina. A lapping fixture was used to ensure that the ends of the compression samples remained flat and parallel. However, it was found that significant rounding occurred near the edges in the first several specimens. This resulted in non-uniform deformation and duplex slip in crystal B, and so a second fixture was devised (Fig. 12). The top and bottom surfaces of this jig were machined flat and parallel, and four v-grooves were cut perpendicular to these surfaces. Two compression specimens were clamped in this jig at a time. This jig was successful in providing flat, parallel loading surfaces, and the difference in bicrystal height varied by less than 12 µm over the end of a given bicrystal sample. Dimensions were easier to maintain over the long bicrystal sides, and these faces were typically parallel to within 10 µm. One corner of crystal A in each bicrystal was chamfered slightly as a reference mark for subsequent indexing required in slip trace analyses (Fig. 8). A final verification of the bicrystal orientation was was made using Laue back reflection. A working distance of 5 cm was used, and the measurement errors were typically ±0.5°.

5.2 Compression Testing

Compression tests were carried out on a standard screw-driven Instron testing machine, and tests were performed at RT and at 660 °C in air. For tests at 660 °C, a resistance furnace was closed around the rams, which were allowed to reach the test temperature before inserting the specimen. This minimized the time that the specimen was at temperature in air, since the formation of an oxide layer has been shown to affect the deformation characteristics of NiAl [56]. Once the test temperature was achieved, the furnace was quickly opened, the specimen was inserted, and the furnace was once again closed. The specimen was allowed to reach thermal equilibrium under a pre-stress of 20-30 MPa, and this typically took 20-30 minutes. A nominal strain rate of 1.5×10^{-4}/sec
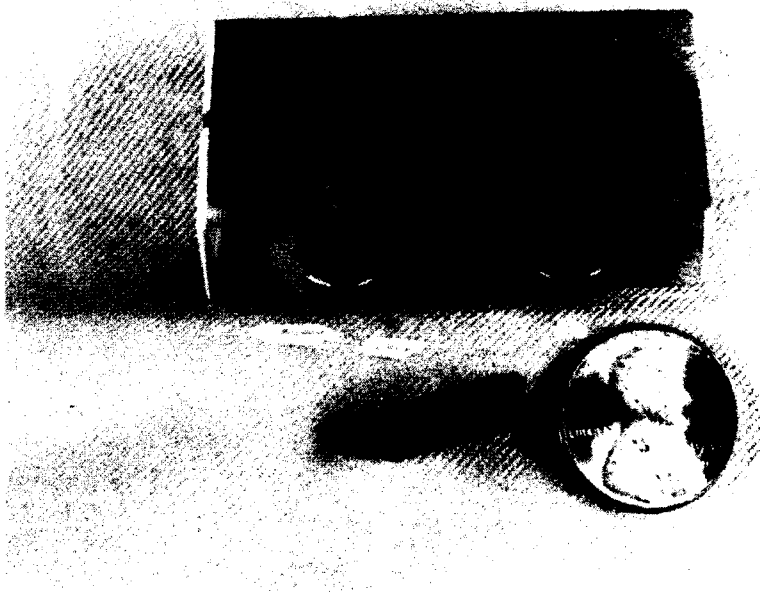
Figure 12   The lapping jig used to produce flat, parallel ends on the compression samples.

was applied, and a total strain of 0.5% to 2.5% was imposed. To preserve the elevated temperature deformation microstructure, the specimens were rapidly cooled with a stream of compressed air ~10 seconds after stopping the crosshead, and were removed as quickly as possible from the furnace. The yield stress, yield character, and total imposed strain were recorded.

5.3 Slip Trace Analysis

After compression testing, Laue back-reflection was used to determine the orientation of each of three orthogonal faces for each crystal in a bicrystal compression specimen. Slip traces were observed for crystal A and crystal B on each of the four long sides of the compression sample using an optical microscope. The mount holding the bicrystal was placed on a rotating stage with a scale marked in one degree increments, and this was used in conjunction with a vernier scale capable of measuring rotations of the stage to a tenth of a degree. The rotating stage was set at 0°, and a straight reference line available on one of the microscope reticles was aligned with the long edge of the bicrystal. The specimen was then rotated until the slip traces were aligned with this reference line, and the angle on the rotating stage was recorded. This measurement defined the angle between that particular slip trace and the edge of the bicrystal specimen, which was parallel to the compression axis. After recording the angles for each of the slip traces on all eight faces (four faces each for crystal A and crystal B), a two-surface slip trace analysis was carried out using standard techniques. The possible slip planes for each crystal were recorded.

5.4 TEM Foil Preparation

Slices were cut from the bicrystal samples in a number of orientations, including slices in the slip plane and slices normal to the compression axis. Slices parallel to the observed slip plane were taken from near the center of the specimen to maximize the chance

of containing the grain boundary, while slices normal to the compression axis were typically taken from a region of crystal A remote from the grain boundary. The slices were cut using wire EDM to a thickness of 500-800 μm, and the slices were gently ground on 600 grit paper to remove the recast layer to a final thickness not less than 300 μm. Thinner foils were initially attempted, but foil damage was clearly evident in discs ground to 150 μm. A light macro-etch of Marble's reagent was used to determine the presence or absence of a grain boundary, and a 3 mm EDM plunge tool was centered over the grain boundary to produce TEM discs. Foils were also produced from slices which did not contain a grain boundary, and the crystal from which the foil was made was determined from Laue back-reflection and a knowledge of the orientation from which the slice was removed from the sample. Mechanical dimpling of the discs prior to electro-chemical thinning was attempted initially to improve the chance of containing the grain boundary within the thin area. However, this was found to be ineffective, and subsequent foils were prepared by electro-chemical thinning alone. An electrolyte of 250 ml methanol, 150 ml butyl cellusolve, and 16-18 ml of perchloric acid (70% concentration) was used at -40 °C. A Fishcione unit was operated at a potential of 20 V, which resulted in a direct current of 8-10 mA. Polishing times ranged from 1-2 hours for these thick samples.

5.5 TEM Analysis

A JEOL 2000FX TEM using a LaB$_6$ filament and operating at 200 kV was used for all microscopy. The double tilt specimen stage allowed ±60° tilt about the axis of the specimen holder, and was modified to allow ±45° tilt about the second axis. A complete determination of the Burgers vector was made using standard dislocation image contrast techniques [61]. Each of the <200> and <110> diffraction vectors available were used in the analyses, and the appropriate <211> vectors were used for final verification. The line direction was determined for all foils, and this was coupled with the Burgers vector to determine the dislocation character (edge or screw). General features of the deformed

51

microstructure were recorded.

Image simulation has often been used in TEM studies of NiAl [5,13,34]. However, if the dislocation line vector occurs normal to a plane of elastic symmetry (ie, along a <100> or <110> direction), then the dislocation images resulting from pure edge or pure screw dislocations in an elastically anisotropic cubic material will appear as if the material were elastically isotropic [61,62]. The vast majority of dislocations observed satisfied these requirements, and so image simulation was not required for a clear determination of the Burgers vector.

Since the TEM foils were cut parallel to the observed slip plane, the dislocation line vectors were expected to lie parallel to the foil surface. In such a case, the contrast from a dislocation will depend not only on the magnitude of $\mathbf{g \cdot b}$ and $\mathbf{g \cdot (b \times u)}$ (for edge or mixed dislocations), but will also depend on the depth of the dislocation in the foil and the magnitude of the effective extinction distance ξ_g. These last two dependencies can lead to an arbitrary interpretation of the dislocation contrast, since ξ_g depends upon the magnitude of s_g, and a given dislocation may exhibit markedly different contrast for a small change in s_g.

To overcome this experimental difficulty, all $\mathbf{g \cdot b}$ analyses were performed using weak beam (WB) imaging techniques, since dislocation contrast in WB is essentially independent of the depth of the dislocation in the foil [63]. When some doubt remained, usually due to low intensity of the dislocation image, the results were corroborated with bright field observations. For maximum contrast and resolution in WB, the value of s_g is required to be

$$s_g \geq 0.2 \text{ nm}^{-1} \quad [63] \tag{19}$$

However, if maximum resolution of the fine details of a dislocation image are not required, then the minimum criterion that must be met for a valid WB image is

$$w = |(\xi_g)(s_g)| \geq 5 \quad [63,64] \tag{20}$$

Although the resolution and the contrast are somewhat reduced for this condition when

52

compared to the requirement in Eqn. (19), the resulting signal is much stronger [63]. This is entirely adequate for a simple $g \cdot b$ analysis, and is, in fact, preferred in the current investigation. Therefore, the criterion for WB imaging in Eqn. (20) was used to determine the magnitude of s_g. Combining this equation with

$$s_g = |g|^2 (\lambda/2)(n-1) \quad [65] \tag{21}$$

allows the parameter n to be determined, so that the g/ng condition for a given diffraction vector which satisfies Eqn. (20) may be specified. The values of n calculated from Eqn. (21) for the three diffracting vectors used in the analyses are given in Table 4, along with the values of n employed in all image analyses (n_{exp}). The value of s_g calculated by inserting (n_{exp}) into Eqn. (21) is also provided in Table 4. Note that $\lambda = 2.51 \times 10^{-3}$ nm for 200 keV electrons.

Three consistent conditions of "effective invisibility" were recorded in each $g \cdot b$ analysis. The Burgers vector may be determined directly when the dislocation is invisible for two unique diffracting vectors g_1 and g_2, and is calculated as the cross product of g_1 and g_2. However, as mentioned earlier, complete invisibility is achieved in general only when both $g \cdot b$ and $g \cdot (bxu)$ are zero. For a pure edge dislocation, these two conditions are satisfied for only one unique diffraction vector, that is, when g is parallel to the dislocation line vector u. Therefore, only one diffracting condition will result in complete invisibility, and other images where $g \cdot b$ is zero are expected to show weak residual contrast due to a non-zero value of $g \cdot (bxu)$. A third consistent condition of "effective invisibility" was therefore utilized in these analyses to remove any doubt concerning the interpretation of the contrast recorded in the images.

53

Table 4. Parameters for calculating weak beam image conditions.

g	$|g|$ (nm^{-1})	ξ_g $(nm)^*$	$n \geq$	n_{exp}	(s_g) (nm^{-1})
<200>	6.944	64.9	2.3	3	0.121
<110>	4.911	44.9	4.7	5	0.121
<211>	8.505	81.2	1.7	2	0.091

* The values of ξ_g were determined from the program "Diffract", which was kindly supplied by Prof. H. Fraser

CHAPTER VI

RESULTS

6.1 Sample Preparation

Bulk analyses were performed to measure the concentration of Ni and Al, and the level of impurities of Si, Ti, V, Cr, Mn, Fe, Co, Y, Nb, Mo, Hf, Ta, and W were also determined. The level of impurities detected for Si (1500 ppm) and Zr (<1000 ppm) are typical for investment cast NiAl. The only other metallic impurity detected was Mg (< 100 ppm). The bulk composition of the NiAl single crystal used throughout the experimental portion of this work was determined to be 49.7% (atomic) Ni, 50.1% Al and 0.2% Si. Other impurities measured were O (70 ppm), C (25 ppm), N (20 ppm) and S (5 ppm). Impurity levels reported in ppm are by weight.

Bicrystals bonded in the MTS machine were produced after 5.2% strain in the [232] bicrystal and 6.5% strain in the [353] bicrystal. The Mo bonding jig produced satisfactory bicrystals with much smaller strains. The [232] bicrystal produced by this technique, designated as [232]-A, was produced after a strain of 0.3%, and the [353] bicrystal bonded in the Mo jig, designated as [353]-A, was produced after 1.0% strain. Optical micrographs of the bonded interface on polished bicrystal specimens typically showed a flat boundary perpendicular to the compression axis. However, several of the bicrystals bonded in the MTS machine exhibited a grain boundary that was locally non-planar. TEM analysis revealed that these regions were characterized by low-angle sub-boundaries parallel to the bonded interface, and the misorientation across these sub-boundaries was less than 3° in all cases. These sub-boundaries are most likely the result of recrystallization due to the large strain concentrated at the interface during the bonding operation. This feature was not

55

observed, either optically or in the TEM, for the [232]-A and [353]-A bicrystals which were produced with much lower bonding strains.

The orientation of each bicrystal specimen was measured using Laue back-reflection prior to testing to ascertain that the desired crystallographic relationship was maintained after bonding and machining. In all cases, the orientation of crystal A was within 1° of the desired [001] axis, and was generally less than 0.5° away from the intended axis. The compression axes for crystal B in each of the [232] and [232]-A bicrystals were within 0.5° of the aim orientation for all but the [232]-A11 specimen, which was 1.0° away from the desired compression axis. However, the compression axes for crystal B in the [353] and [353]-A bicrystals were 1-2° from the desired direction, and these bicrystals possessed a compression axis closer to [474]. Note that the observed deviation from the desired [353] axis increased the tilt angle between the [232] and the [353] bicrystals. The x_A and x_B axes were parallel to within 2° in all cases.

The orientation of the bicrystal faces was determined for subsequent slip trace analyses. Fortuitously, the faces were very nearly parallel to the $(100)_A$ and $(010)_A$ planes in crystal A for both the [232]-A and [353]-A bicrystals, so that the corresponding faces in crystal B were the $(10\bar{1})_B$ and $(3\bar{4}3)_B$ planes, respectively. Therefore, the $[010]_B$ Burgers vector expected to operate in crystal B is wholly contained in two opposite faces of this crystal (see Fig. 9 and Fig. 10), and the passage of these dislocations will cause no offset on the $(10\bar{1})_B$ and $(\bar{1}01)_B$ faces. This made slip trace analysis difficult in crystal B, especially at low strains, since traces on two adjacent faces are required to determine a slip plane. The faces for the [232] and [353] bicrystals were nearly parallel to the $(110)_A$ and $(1\bar{1}0)_A$ planes.

6.2 Compression Testing

All of the [232] and the [353] bicrystals yielded smoothly, but the two [232] bicrystals tested at RT exhibited stable cracking, and an associated load drop, after about

1% strain. All of the [232]-A and [353]-A bicrystals also yielded smoothly, but at RT these samples exhibited a discernable change in slope just past yield on the load/elongation plot. The flow stresses were typically 220 MPa at RT and 150 MPa at 660 °C. The first [232]-A and [353]-A bicrystals tested at 660 °C (specifically, [232]-A9 and [353]-A4) exhibited large, irregular load drops just after yield. Visual inspection of these two specimens showed extremely localized deformation concentrated in one distinct slip band which "originated" at an edge of crystal B next to the compression platen, and extended until it emerged just above the grain boundary. The amount of uniform strain was estimated by subtracting the offset on the load/elongation plot associated with the irregular load drops. Nearly all of the deformation in these samples was concentrated in the slip band, and very little uniform deformation occurred. About 3 mm was removed from the end of crystal B in the two remaining [232]-A and [353]-A samples tested at 660 °C, so that this band would intersect the grain boundary. These samples possessed an overall aspect ratio of about 2.4:1, although the aspect ratio for crystal B was less than 1:1. The flow stress for these bicrystals increased by ~10%, and enhanced uniform flow was observed after yield, although in both cases localized flow still occurred. In each of these last two bicrystals, the intense slip band intersected the bicrystal boundary. A summary of the data from the compression tests is provided in Table 5.

6.3 Slip Trace Analysis

Two-surface slip trace analyses were performed on all deformed bicrystals. Consistent with accepted practice, slip traces on one surface that were clearly associated with slip traces on an adjacent face were required to define a slip plane. Results from the slip trace analyses are included in Table 5.

Table 5. Data summary for bicrystal compression tests and slip trace analyses.

SPEC #	T (°C)	l/d	ε (%)	SLIP PLANE Crystal A	SLIP PLANE Crystal B	COMMENTS
232-2	RT	2.2	1.2	None	(101) D*	Cracking, gb kinking
232-3	RT	2.2	1.3	None	(101) D, (210)	Cracking, gb kinking
232-A5	RT	2.9	1.1	None	Not Determined	
232-A10	RT	3.0	0.6	None	(101) D	Cut for TEM
353-A7	RT	2.8	1.6	None	(101) D	Cut for TEM
353-A10	RT	3.0	0.5	None	Not Determined	Cut for TEM
353-A11	RT	2.9	1.7	None	(101) D	$\dot{\varepsilon} = 1.5 \times 10^{-2}$
232-1	660	2.2	0.8	(011), (0$\bar{1}$1)	(101)	Cut for TEM
232-A9	660	2.9	1.3	None	(101) ISB**	$\varepsilon_{unif} = 0.4\%$
232-A11	660	2.4	2.5	(001) D, (011) GB	(101) ISB, (010) D	$\varepsilon_{unif} = 1.6\%$, cut for TEM
353-3	660	2.5	1.1	(101), ($\bar{1}$01), (011), (0$\bar{1}$1)	(101) D, (010)	
353-A4	660	3.0	1.0	None	(101) ISB	$\varepsilon_{unif} = 0.2\%$
353-A5	660	2.4	1.0	(001) D, (011) GB	(101) ISB, also D	$\varepsilon_{unif} = 0.5\%$, cut for TEM

* Dominant slip trace

** Trace of the intense slip band

58

6.3.1 Crystal B

Slip traces were easily evident in crystal B for all of the specimens tested, but a slip plane could not be determined in two of the specimens tested at RT ([232]-A5 and [353]-A10), since slip traces were not evident on two orthogonal faces. The two (parallel) faces which displayed no slip traces were the $(\bar{1}01)_B$ and $(10\bar{1})_B$ planes. Furthermore, the traces measured on the remaining two faces were along the $[\bar{1}01]_B$ direction. Both of these observations are consistent with slip occurring on the expected $[010]_B(101)_B$ slip system in these two bicrystals. The expected $(101)_B$ slip plane in crystal B was the dominant slip plane in all but one of the remaining bicrystal samples, although several of the specimens exhibited weak secondary slip traces as well. In particular, the $(010)_B$ plane was determined to be active in two bicrystals tested at 660 °C, and it is possible that cube slip along either the $[100]_A$ or $[001]_A$ direction occurs on this plane. Note that these slip vectors are well aligned with the $[\bar{1}11]_A$ and $[111]_A$ slip vectors in crystal A, respectively.

Characteristics of the intense slip band are shown in Fig. 13. In each case, the intense slip band occurred on the $(101)_B$ plane. The traces on the $(10\bar{1})_B$ face were very straight, and the displacement normal to the adjacent $(3\bar{4}3)_B$ face is clearly seen in Fig. 13(a). No significant displacement normal to the $(10\bar{1})_B$ face occurred, as evident by the fact that the crystal face is in focus on both sides of the slip plane. Optical microscopy at the edge of the orthogonal $(3\bar{4}3)_B$ face confirmed this observation, as shown in Fig. 13(b), and the slip traces on this face are wavy. These observations suggest that the dislocations which operate in this slip band are $[010]_B$, and the character of the traces suggest that the dislocations have a screw orientation.

6.3.2 Crystal A

Traces were observed in crystal A for every specimen tested at 660 °C, but traces were typically absent in the bicrystals tested at RT. When slip was evident in crystal A at RT, the traces occurred only on the $(010)_A$ and $(0\bar{1}0)_A$ faces, and the traces occurred along
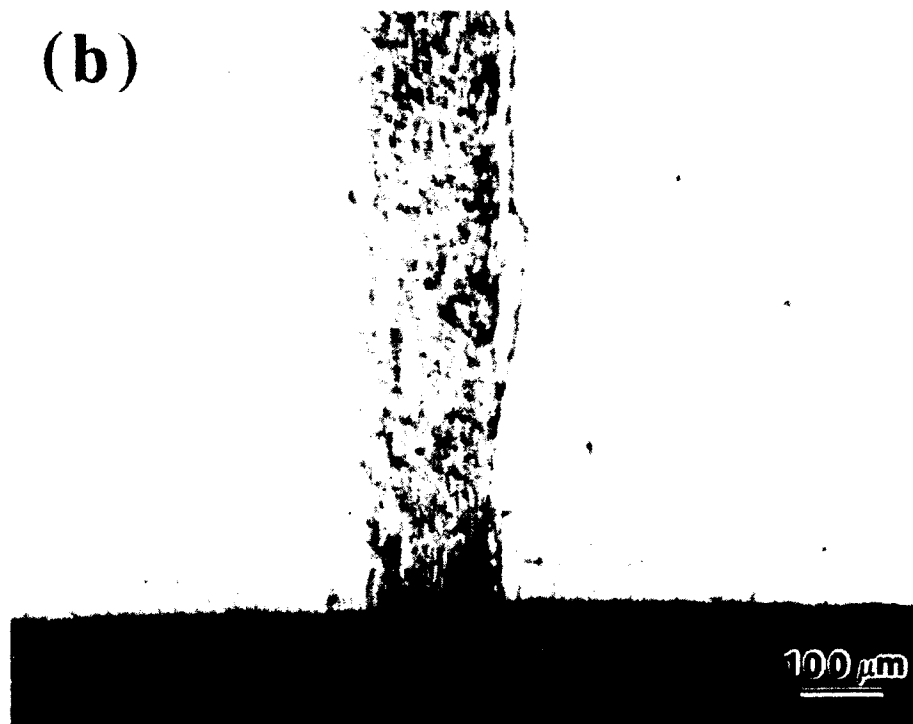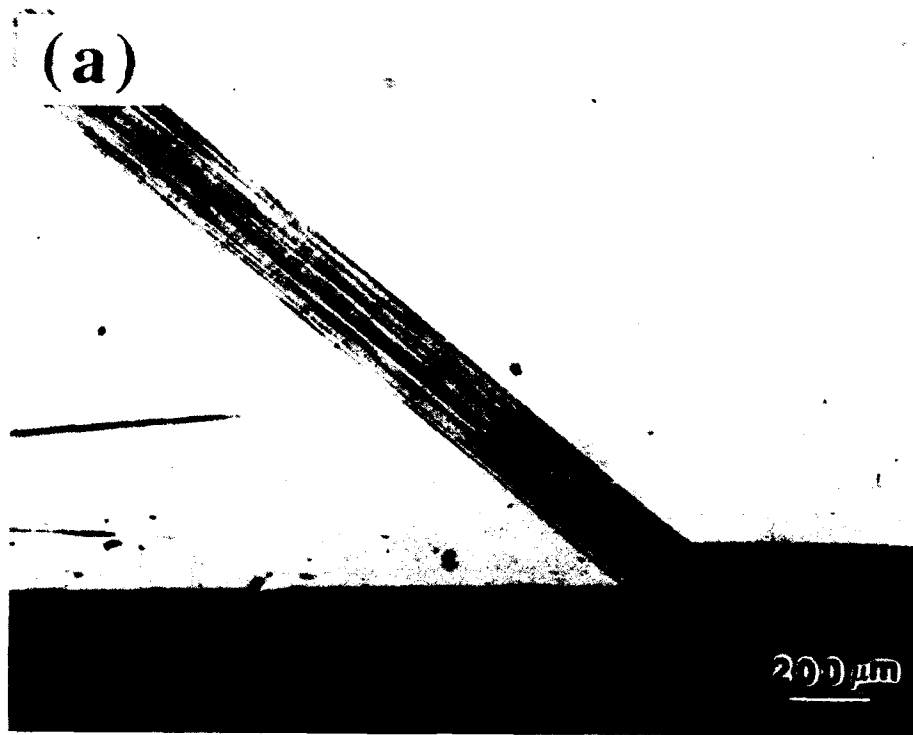
Figure 13 Features of the intense slip band as seen on (a) the $(10\bar{1})_B$ face, and (b) the $(3\bar{4}3)_B$ face. The specimen shown is [353]-A4, tested at 660 °C.

the $[100]_A$ direction. Therefore, these traces are consistent with slip occurring in crystal A on a plane in the [100] zone. The absence of slip traces on the $(100)_A$ and $(\bar{1}00)_A$ faces suggests that the Burgers vector of the active dislocations belong to the [100] zone.

A slip plane could not be defined for two of the bicrystals tested at 660 °C ([232]-A9 and [353]-A4), since very little uniform deformation occurred in these bicrystals, as discussed above. However, planes were clearly defined in bicrystals [232]-A11 and [353]-A5, where the intense slip band intersected the grain boundary and enhanced uniform flow occurred (Fig. 14). Coarse, wavy traces dominated crystal A in each of these bicrystals. These traces were aligned roughly along the $[100]_A$ and $[010]_A$ directions on the $(010)_A$ and $(100)_A$ faces, respectively, but the traces varied from these directions by as much as 10° near the edges of the bicrystal sample which were parallel to the compression axis. These traces were taken to define dislocation activity (either glide or climb) on the $(001)_A$ plane. The wavy nature of these traces implies that prolific cross-slip is occurring if the traces result from the glide of dislocations, or that dislocations are climbing on more than one plane.

These coarse traces were altogether absent in a region extending 1-2 mm from the grain boundary (see region (B) in Fig. 14(b)). Very fine, straight traces were discerned in this region, and these traces defined the slip plane in crystal A which was parallel to the dominant slip plane in crystal B. Specifically, in [232]-A11 the $(0\bar{1}1)_A$ plane was observed in this boundary region, which is parallel to the dominant $(010)_B$ slip plane in crystal B, and in [353]-A5 the $(011)_A$ plane was observed, which is parallel to the dominant $(101)_B$ plane in crystal B.

It is interesting to observe that slip is not transmitted across the grain boundary where the intense slip band intersects the bicrystal interface, but appears to be "reflected" (Fig. 14). However, slip did was transmitted across the interface ahead of the intense slip band in [353]-A5.
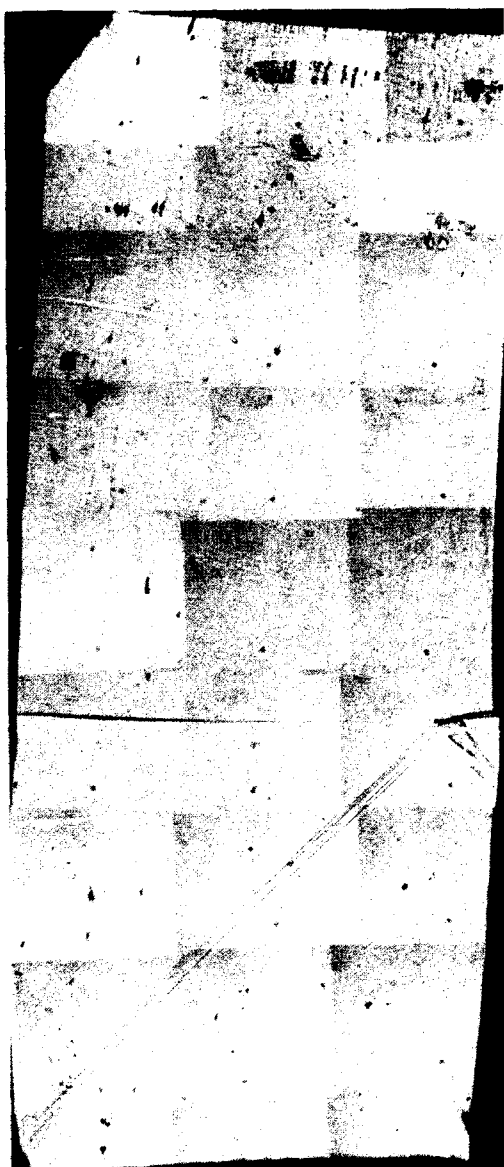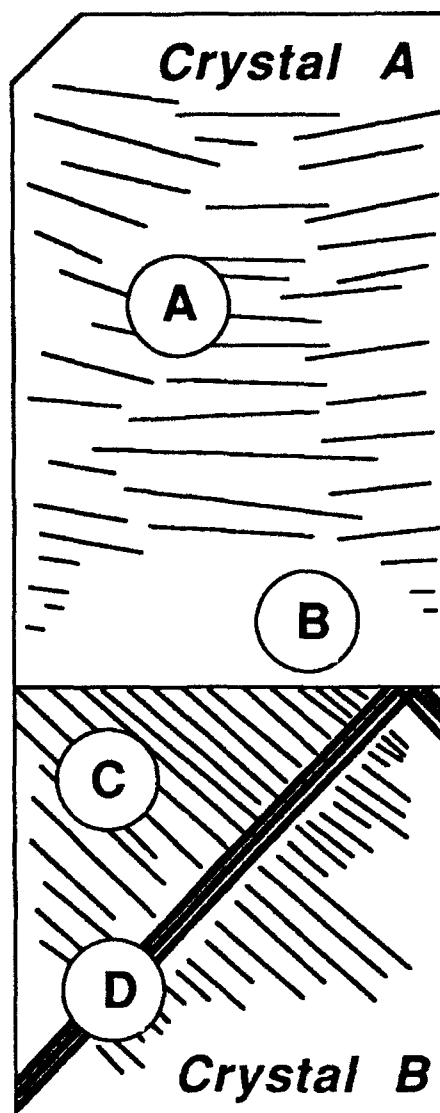
(a)   (b)

Figure 14   Slip traces on specimen [232]-A11 shown on (a) a composite micrograph and (b) a schematic drawing illustrating the main features. These features include (A) coarse slip markings in crystal A roughly aligned along $(001)_A$, (B) the region of fine slip traces along the $(0\bar{1}1)_A$ plane (not visible in Fig. 14(a) at this magnification), (C) dominant slip traces along $(010)_B$, and (D) the intense slip band along $(101)_B$. The bicrystal is 5 mm wide and 12 mm high in (a).

The observed slip traces in the |232|-1 sample were significantly different than the slip described for the [232]-A and [353]-A bicrystals. Extensive multiple slip is clearly evident at the grain boundary in crystal A after deformation at 660 °C, and the coarse traces defining the $(001)_A$ plane were completely absent. A micrograph of the slip traces at the boundary of [232]-1, deformed 0.8% at 660 °C, is shown in Fig. 15. Single slip on the $(101)_B$ plane is distributed homogeneously across crystal B, and duplex slip is clearly evident in crystal A. The results of the two-surface slip trace analyses show these two planes to be the $(011)_A$ plane, which is nearly contiguous with the $(101)_B$ slip plane in crystal B, and the $(0\bar{1}1)_A$ plane. These are the two planes predicted to operate in crystal A based on the calculations in Chapter III. It is important to observe that no resolved shear stress is calculated on these planes along the $[100]_A$ direction, but that $\tau_{crss}^{<111>}$ is exceeded along the two <111> Burgers vectors contained within each of these planes at RT.

Highly localized deformation was observed in crystal A at the grain boundary after deformation at RT in those bicrystals where recrystallization had occurred. This deformation appeared to be related to the phenomenon of kinking known to occur in single crystals of NiAl aligned along a cube axis, and may have initiated in the recrystallized regions, where some rotation of the crystal had occurred, as described in Section 6.1.

6.4 TEM Analysis

Six of the deformed bicrystals were sliced for TEM investigations, as indicated in Table 5. In addition, the repre⸱ ntative microstructure of an undeformed sample was investigated in an as-bonded bicrystal. A total of forty-one foils were produced from these seven bicrystals, and the results that follow represent investigations on nearly half of these foils.

In general, the foils polished reasonably well, and typically exhibited a significant amount of usable thin area. Several foils had a number of bend contours, and three foils
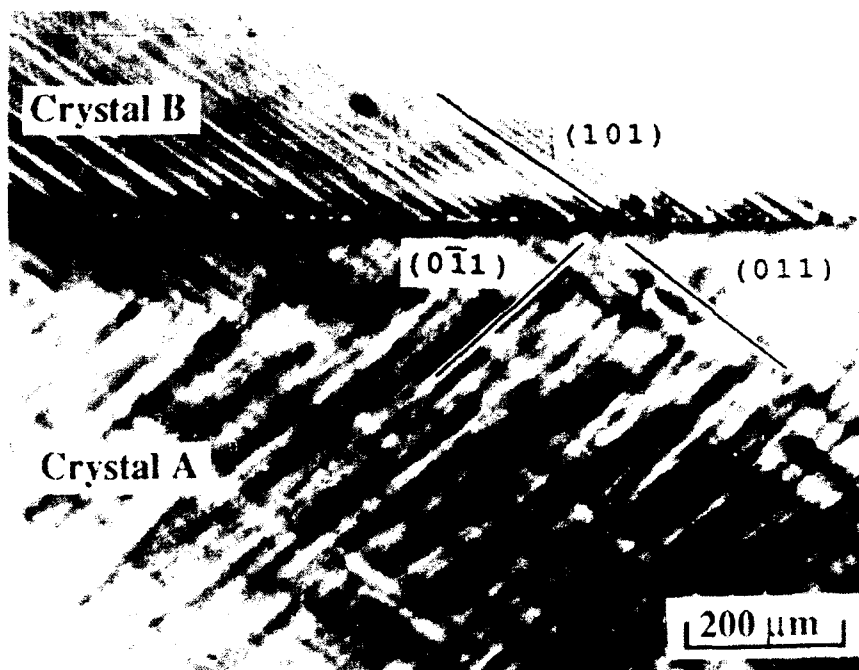
Figure 15   Micrograph of [232]-1, tested at 660 °C, showing the slip traces on the $(101)_B$ plane in crystal B and duplex slip on the $(011)_A$ and $(0\overline{1}1)_A$ planes in crystal A.

had no thin area at all. In some cases, a mild etching effect occurred which resulted in a "cored" contrast that was evident only at low magnifications. The thick outer ring surrounding the electropolished region of the foils resulted in robust samples which were relatively insensitive to repeated handling. The bicrystal grain boundary was contained in only one foil, and that foil possessed no thin area at all. This foil was subsequently submitted for ion-milling, and some thin area resulted. However, the dislocation density at the boundary was too high to extract useful information from this specimen.

Analyses were relatively straightforward in the foils sliced from the $(001)_A$ planes in crystal A. The appropriate diffracting vectors from the [001] zone axis (ZA) were used, along with the desired diffraction vectors in the four <110> zones which were 45° from the [001] ZA. Analyses of foils cut along the observed slip plane in crystal A were complicated by the fact that the grain boundary was not contained within the thinned region of the foil as initially intended. In only two bicrystals ([232]-A11 and the undeformed sample) were the slices for TEM foils cut along the $(0\bar{1}1)_A$ plane, which was parallel to the $(010)_B$ plane. For these foils, a foil normal near [010] in the TEM indicated that crystal B had been thinned, while a foil normal of $[0\bar{1}1]$ determined that crystal A had been thinned. However, the remainder of the TEM foils were cut along the $(011)_A$ plane, which was parallel to the $(101)_B$ plane. In either case, a <110> foil normal was observed, and the only way to differentiate between crystal A and crystal B was to determine the relationship of the grain boundary trace to the observed <110> selected area diffraction pattern (SADP), as illustrated in Fig. 16.

To overcome this difficulty, selected area electron channeling patterns were obtained with the 2000FX in the thick regions of the foil. The foil was translated, and a 90° rotation of the electron channeling pattern occurred when the grain boundary was crossed. A "map" of the grain boundary trace was plotted by following the boundary as it traversed the foil and recording the x- and y- coordinates of the boundary. The crystal which contained the thin region could then be determined by indexing the electron
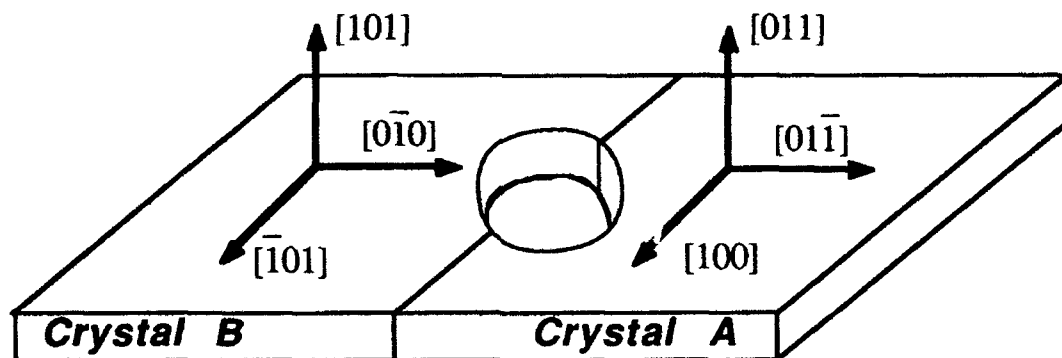
Figure 16   Schematic of the crystallographic relationship between crystal A, crystal B, and the grain boundary in a TEM foil cut along the $(011)_A$ and $(101)_B$ plane.

channeling patterns and relating these to the trace of the grain boundary. In every case, the trace of the grain boundary was determined to lie parallel (within experimental error) to either a <100> or a <110> direction on the electron channeling pattern, and a dislocation microstructure which was characteristic of the grain thus indicated was observed in every case.

The majority of the dislocations imaged proved to be pure edge dislocations, and the line vector u typically occurred along a <100> direction. When imaging a dislocation with a diffracting vector such that g·b and g·(bxu) were zero, the dislocation was completely invisible, and residual contrast due to elastic anisotropy was not observed, as discussed in Section 5.5. However, residual contrast was often present for edge dislocations when g·b was zero, but g·(bxu) was non-zero. This residual contrast was especially strong when the Burgers vector was nearly parallel to the beam direction and g was nearly perpendicular to u, since this configuration maximizes the dot product between the diffracting vector g and the cross product (bxu). As shown in earlier contrast experiments [38,66], a strong double image occurred in the bright field (BF) image for this condition (for example, see dislocation loops A and B in Fig. 25(a)), but a simple distinction between g·b=0 and g·b=2 could be made by either varying s_g [67] or by imaging the dislocation in WB.

The results of the TEM analyses are presented in the following sections.

6.4.1 As-Bonded Specimen

Foils of the undeformed sample were cut along the $(0\bar{1}1)_A$ plane in crystal A and the parallel $(010)_B$ plane in crystal B. The dislocation density was very low in both crystals. Dislocations with [100], [010], and [001] Burgers vectors were observed, and non-<100> dislocations were not seen. Dislocations were typically straight and occurred along <100> directions, and all of the dislocations were edge dislocations. This configuration yields a broad, shallow energy minima for [100] dislocations on the (001) plane at 660 °C

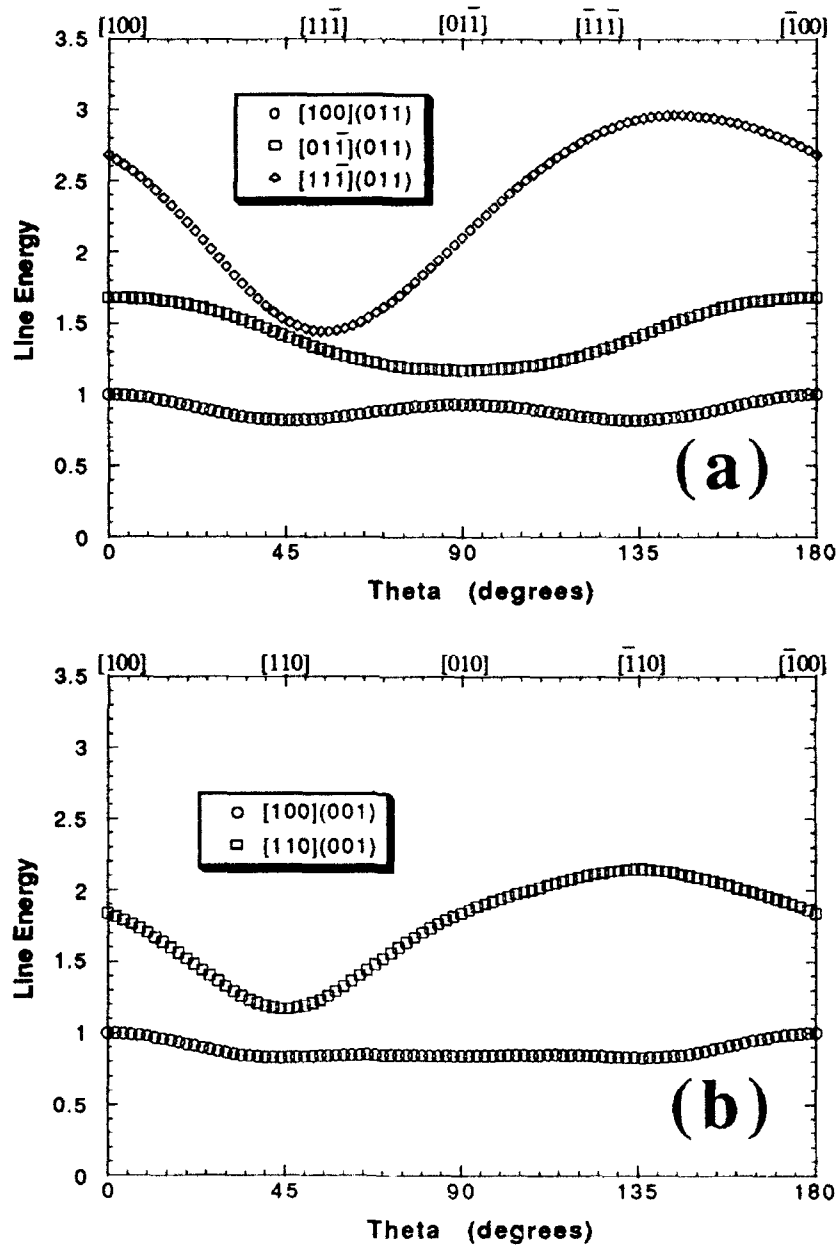Figure 17   Line energy of (a) [100], [01$\bar{1}$], and [11$\bar{1}$] dislocations as a function of dislocation character on the (011) plane at 660 °C and (b) [100] and [110] dislocations as a function of dislocation character on the (001) plane at 660 °C. The horizontal axis is the angle between the dislocation line vector and the [100] direction. The line energy is proportional to $C_{44}(a_0^2/4\pi)\ln(r/r_0)$.

(Fig. 17(b)). Note that mixed [100] dislocations with a line vector near the [11$\bar{1}$] direction on the (011) plane have nearly the same energy (Fig. 17(a)), but these dislocations were not observed. Concentric prismatic dislocation loops were seen infrequently, and these loops had an [001] Burgers vector and occurred on the (001)$_A$ plane in crystal A.

6.4.2   Specimens Deformed at RT

All of the dislocations observed in crystal B after deformation at RT were determined to possess the [010] Burgers vector. The dislocations were typically curved, and were often heavily pinned along the length of the dislocation line (Fig. 18). A large amount of debris in the form of small, often elongated, dislocation loops was also evident.

Dislocations in crystal A of the [232]-A10 bicrystal deformed 0.6% at RT were typically pure edge dislocations with a <100> Burgers vector and a <100> line direction, and several of these are seen in Fig. 19. These dislocations were generally short, since they were not contained in the (011)$_A$ plane of the foil. However, long dislocations which were typically curved at the ends were often observed, and two dislocations typical of this morphology are labeled as A and B in Fig. 19. These dislocations are clearly visible in the BF image of Fig. 19(a), and significant contrast is also evident in the WB images of Fig. 19(b) and 19(c). However, these dislocations are invisible when the diffraction vector is [200], and only weak residual contrast is evident with the [211] and [2$\bar{1}$1] diffraction vectors. This clearly shows that these dislocations have an [01$\bar{1}$] Burgers vector. The line direction of these dislocations is along the [100]$_A$ direction, which is parallel to the grain boundary, and these dislocations possess a strong edge character.

Analyses of [353]-A10 deformed 0.5% at RT show features similar to those described for the [232]-A10 bicrystal. Most dislocations in crystal A were short and straight, and were determined to have a <100> line direction. However, all dislocations analyzed were of the b=<100> type, and non-<100> dislocations were not observed. An extended "pile-up" of dislocation segments was observed, and the length of the dislocation
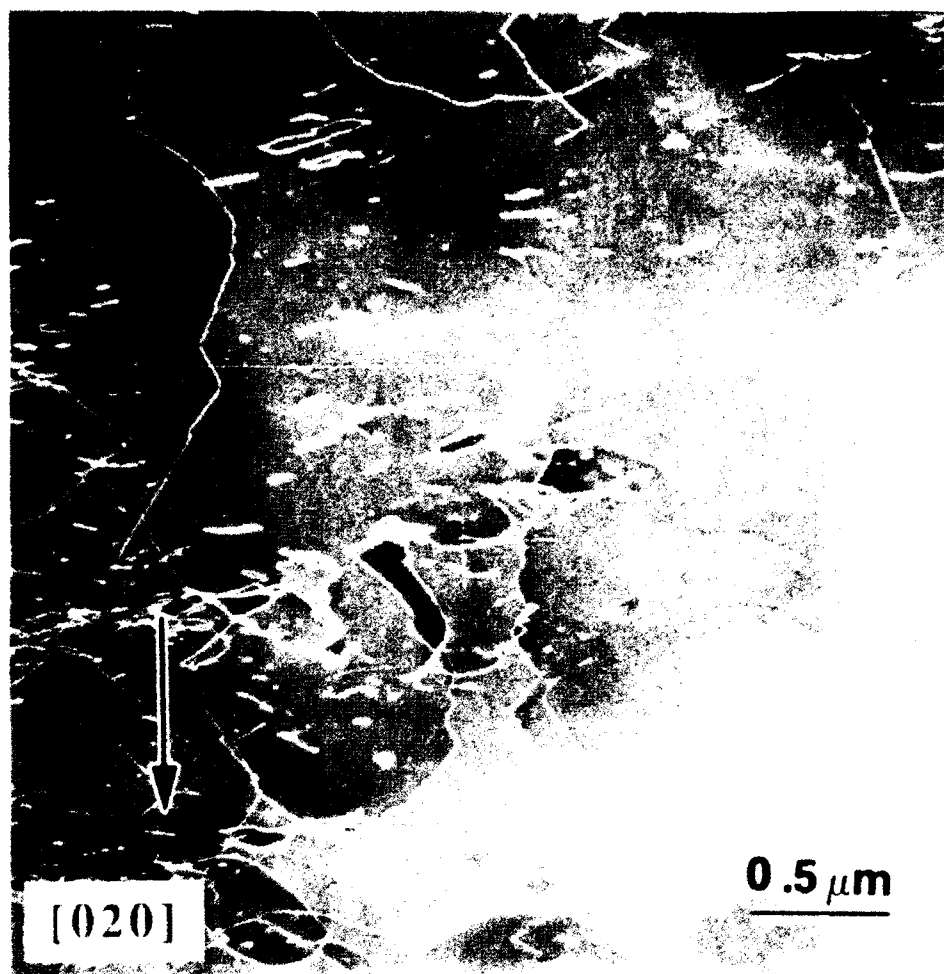
Figure 18   Typical BF micrograph of the dislocation morphology in crystal B after deformation at RT. All dislocations were analyzed as [010] dislocations.

Figure 19   Micrographs of a **g·b** analysis for [232]-A10 deformed 0.6% at RT. Fig. 19(a) is a BF image, and the remaining micrographs are imaged in WB. The dislocations labeled A and B have an [01$\bar{1}$] Burgers vector and lie along the [100] direction, which is parallel to the grain boundary, and dislocation C has a [100] Burgers vector. The foil normal is near [011]$_A$, and the diffracting vectors are indicated.

71

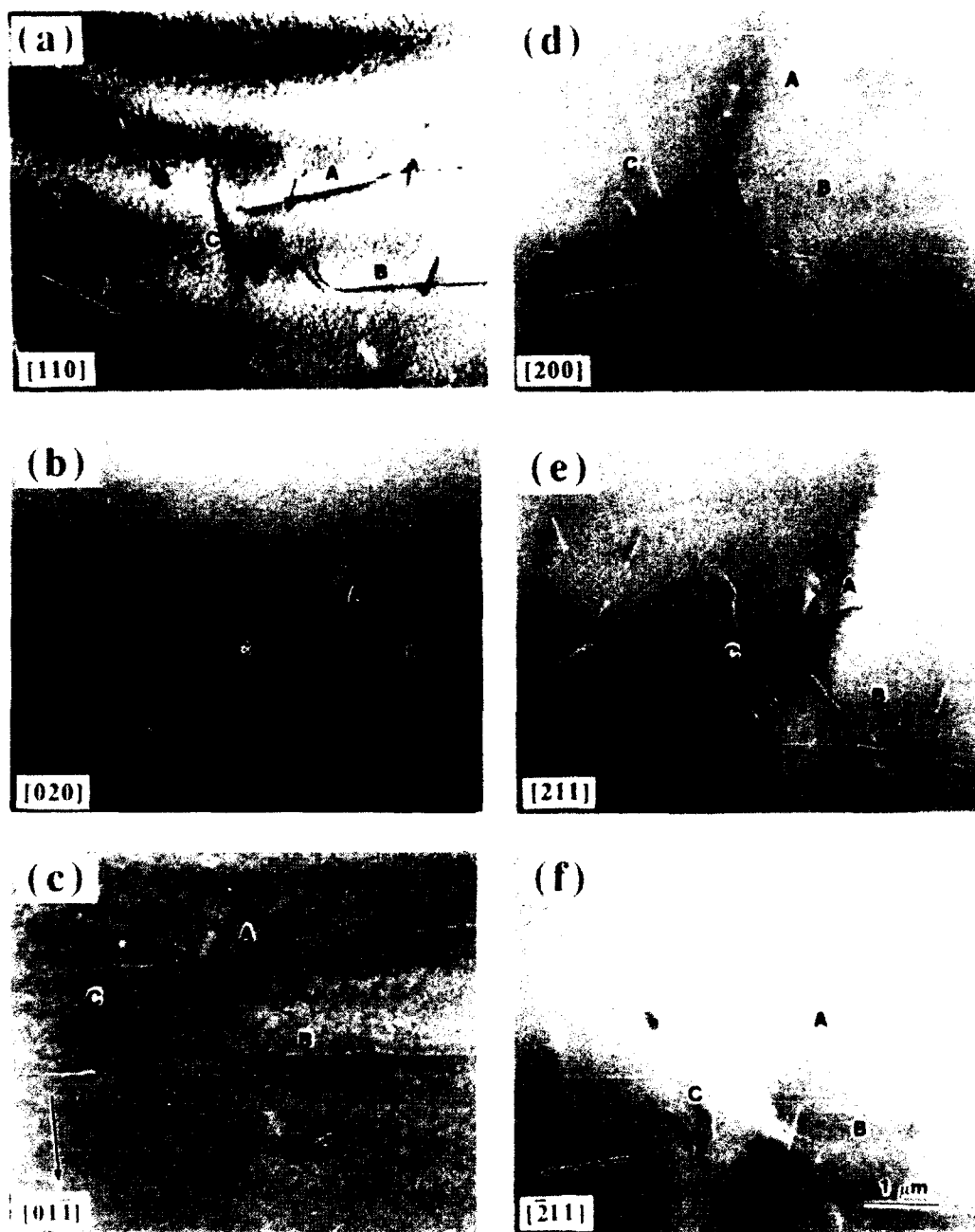segments in this feature was slightly longer than the typical dislocation segment length. These dislocations were analyzed as [010] dislocations with u= [101]. Very few long, slightly curved dislocations were seen, and these were determined to be <100> dislocations.

Additional features were observed in crystal A of the [353]-A7 bicrystal after 1.6% strain at RT. This bicrystal showed a higher density of dislocations, and the majority were short, straight segments of b=<100> edge dislocations. A foil cut along the (001)$_A$ plane showed long, curved lengths of b=<100> dislocations, and in one case a segment which was consistent with a large prismatic dislocation loop was observed. Foils cut in the (011)$_A$ plane also exhibited long lengths of dislocations that were frequently curved at the ends (Fig. 20). Consistent with the analysis in Fig. 19, the long dislocations labeled A-D have a [01$\bar{1}$] Burgers vector, and these dislocations were determined to have a [100] line direction. Dislocation E is an edge dislocation with b=[100] and u=[01$\bar{1}$].

6.4.3 Specimens Deformed at 660 °C

The appearance of the dislocations in crystal B after deformation at 660 °C were generally very similar to that observed after deformation at RT. In addition to the [010] dislocations typically present, dislocations with b=[100] and [001] were also observed. Dislocation loops were a more common feature, and dislocation tangling was often seen. A tendency toward forming broad bands of dislocations also occurred.

Foils from sample 232-1 and 353-A3 were cut from the observed (011)$_A$ slip plane in crystal A, and the dislocation structure near the grain boundary was very similar in these two bicrystals (Fig. 21 and Fig. 22). In each case, the dislocations were typically long and straight, and were generally curved near the ends. Small loops were also frequently seen, and these were often elongated. The g·b analyses presented in Fig. 21 and Fig. 22 clearly show that nearly all of the dislocations have an [01$\bar{1}$] Burgers vector, and the line direction was determined to be u=[100], so that these are edge dislocations. Once again, it
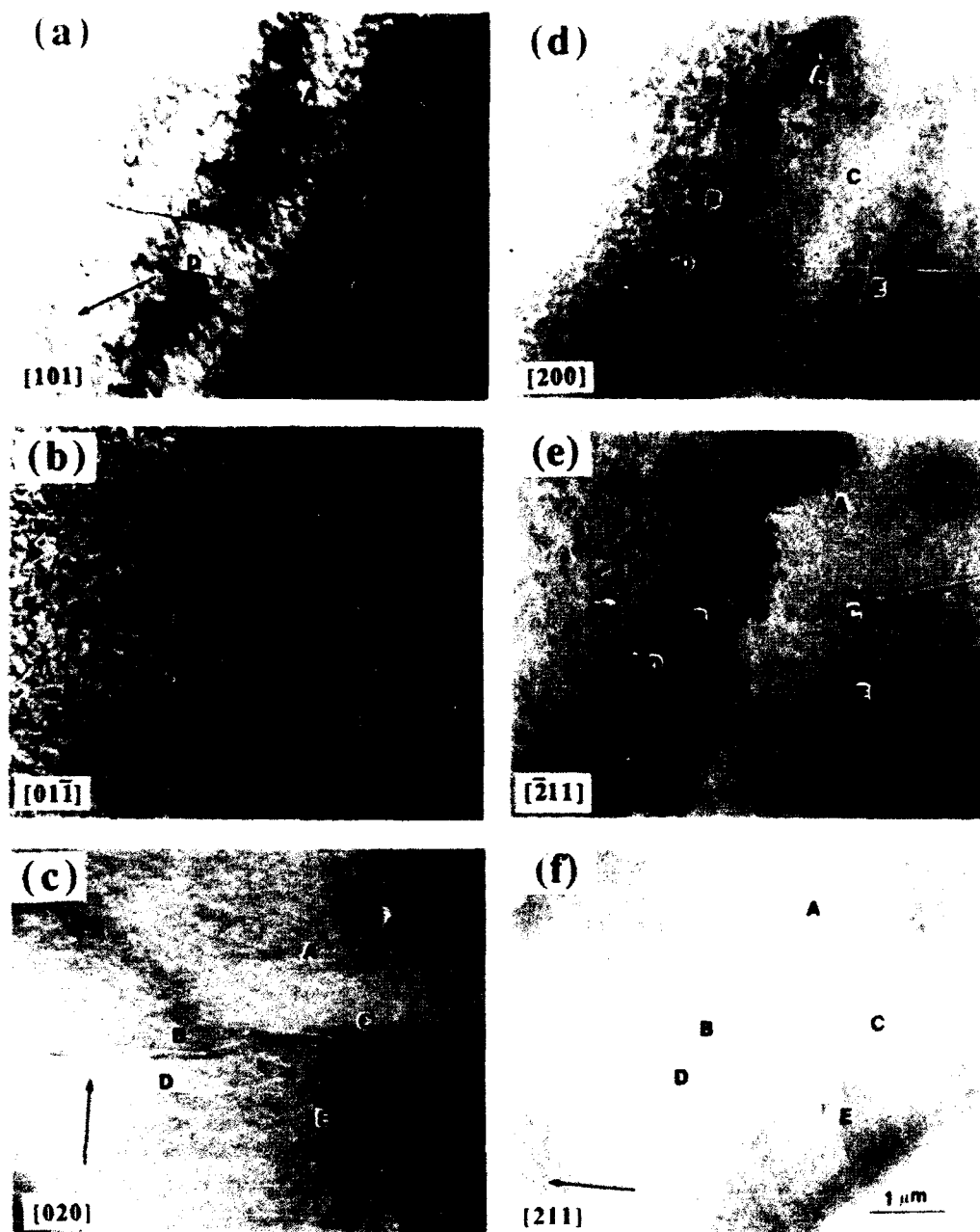
Figure 20   Micrographs of a g·b analysis of dislocations in [353]-A7 deformed 1.6% at RT. Fig. 20(a) is a BF image, and the remaining micrographs are imaged in WB. The dislocations labeled A-D have an [011] Burgers vector and lie along the [100] direction. Dislocation E is a b=[100] dislocation with a line vector of u=[011]. The foil normal is near [011]$_A$, and the diffracting vectors are indicated.

73

Figure 21 WB micrographs of a **g·b** analysis of dislocations in [232]-1 deformed 0.8% at 660 °C. The dislocations labeled A-D have an [01$\bar{1}$] Burgers vector and lie along the [100] direction, which is parallel to the grain boundary. The foil normal is near [011]$_A$, and the diffracting vectors are indicated.

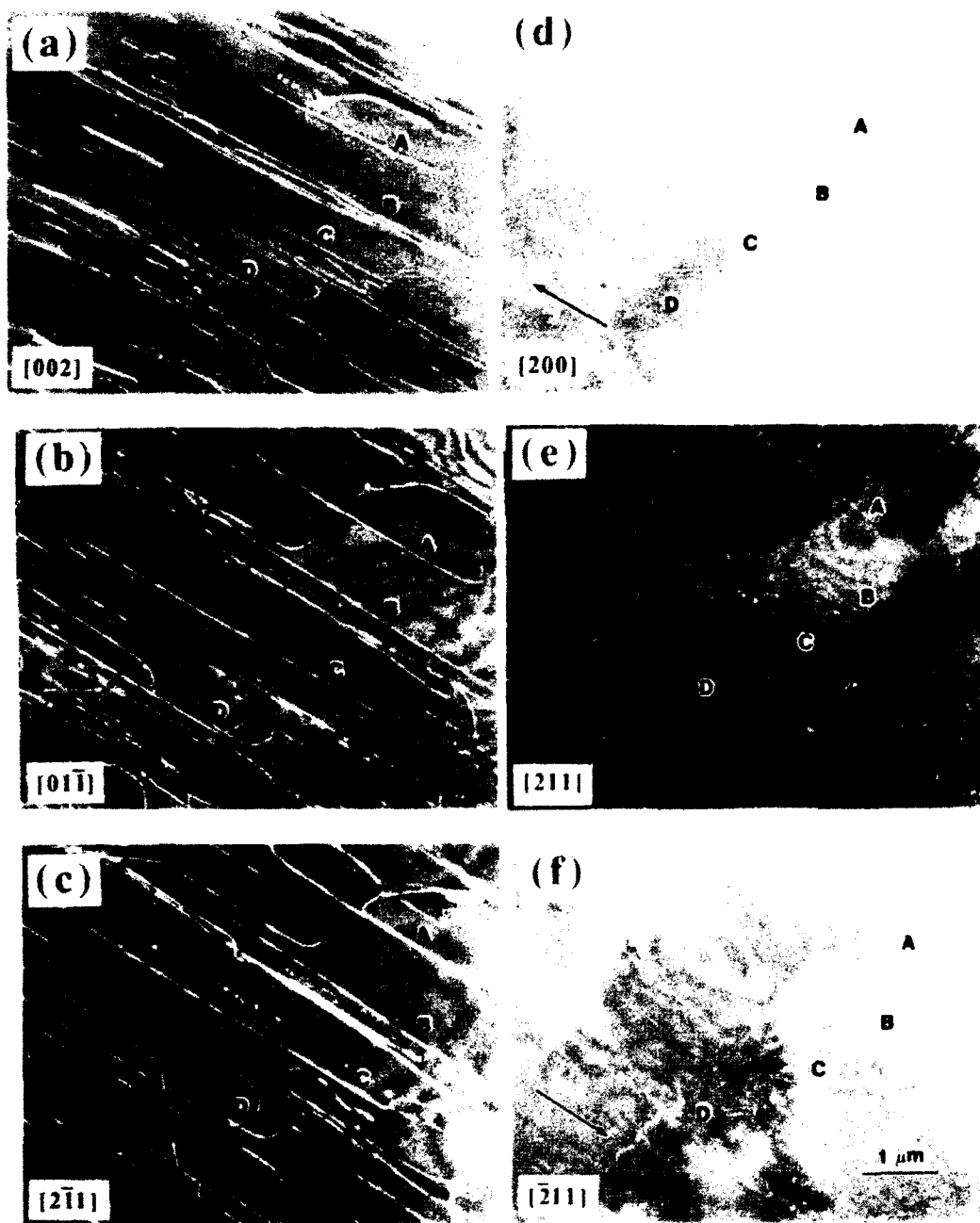Figure 22　WB micrographs of a **g·b** analysis of dislocations in [353]-A5 deformed 0.5% at 660 °C. The dislocations labeled A-D have an [01$\bar{1}$] Burgers vector and lie along the [100] direction, which is parallel to the grain boundary. The foil normal is near [011]$_A$, and the diffracting vectors are indicated.
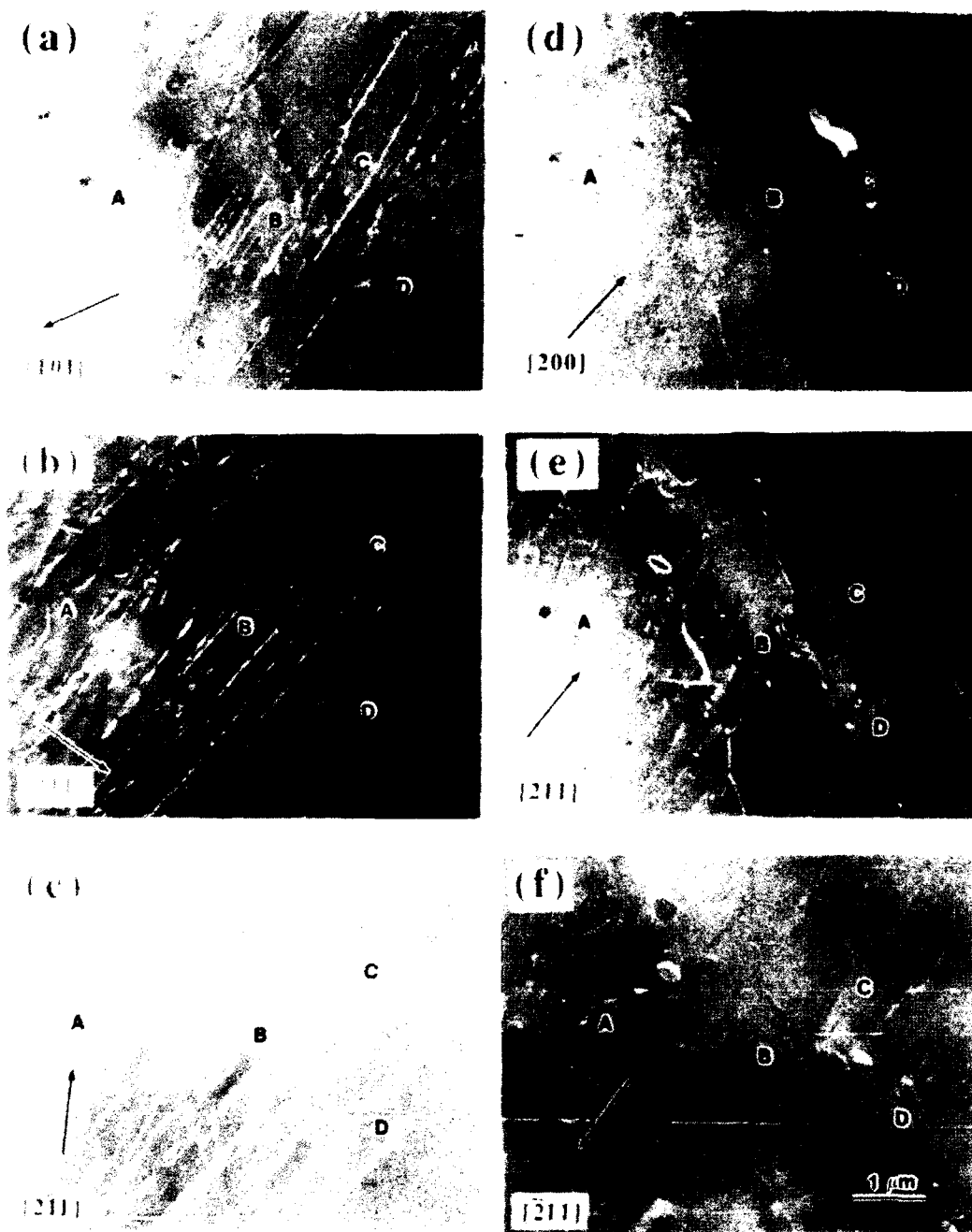
is important to note that these dislocations are parallel to the grain boundary. Tilting experiments were performed to determine the line direction of the curved segments at the end of several dislocations and, while the accuracy of these analyses were not as good as for the long, straight segments, a line direction of $[01\bar{1}]$ was indicated in each case. Therefore, these dislocations lie on the $(011)_A$ plane, and this is consistent with the slip plane deduced from the observed slip traces. Large "kinks" and "double kinks" were also a common feature on the straight segments of $[01\bar{1}]$ dislocations after deformation at 660 °C (for example, see dislocation A in Fig. 22). Finally, dislocation debris in the form of long, heavily jogged dislocations were sometimes observed. An example of these long, irregular dislocations is seen in Fig. 22.

Foils from specimen [232]-A11 were cut from the $(01\bar{1})_A$ plane, which was the observed slip plane at the grain boundary for this sample. The observed features were identical to those just described for samples [232]-1 and [353]-A5 (Fig. 23). However, the majority of the dislocations in this specimen were b=[011], and the line direction was [100]. Analyses of the line direction for the curved segments indicated a line vector of u=[011], and this is consistent with the observed $(01\bar{1})_A$ slip plane. A larger amount of debris was observed, and this correlates well with the larger uniform strain experienced by this bicrystal.

Examination of foils taken from crystal A far (3-5 mm) from the bicrystal interface in the $(001)_A$ plane revealed a completely different microstructure (Fig. 24). Dislocations occurred almost exclusively in concentrated bands aligned along the [100] and [010] directions. The dislocations in these bands had b=[010] and b=[100], respectively, so that all of the dislocations in these bands were pure edge dislocations. This is illustrated in Fig. 25, where two such bands intersect. When imaged with a $[1\bar{1}0]$ diffraction vector, both bands of dislocations are visible (Fig. 25(a)). However, only the [100] dislocations are visible when g=[200] (Fig. 25(b)), and only [010] dislocations are apparent when imaged with the [020] vector (Fig. 25(c)). The dislocations in the bands were very
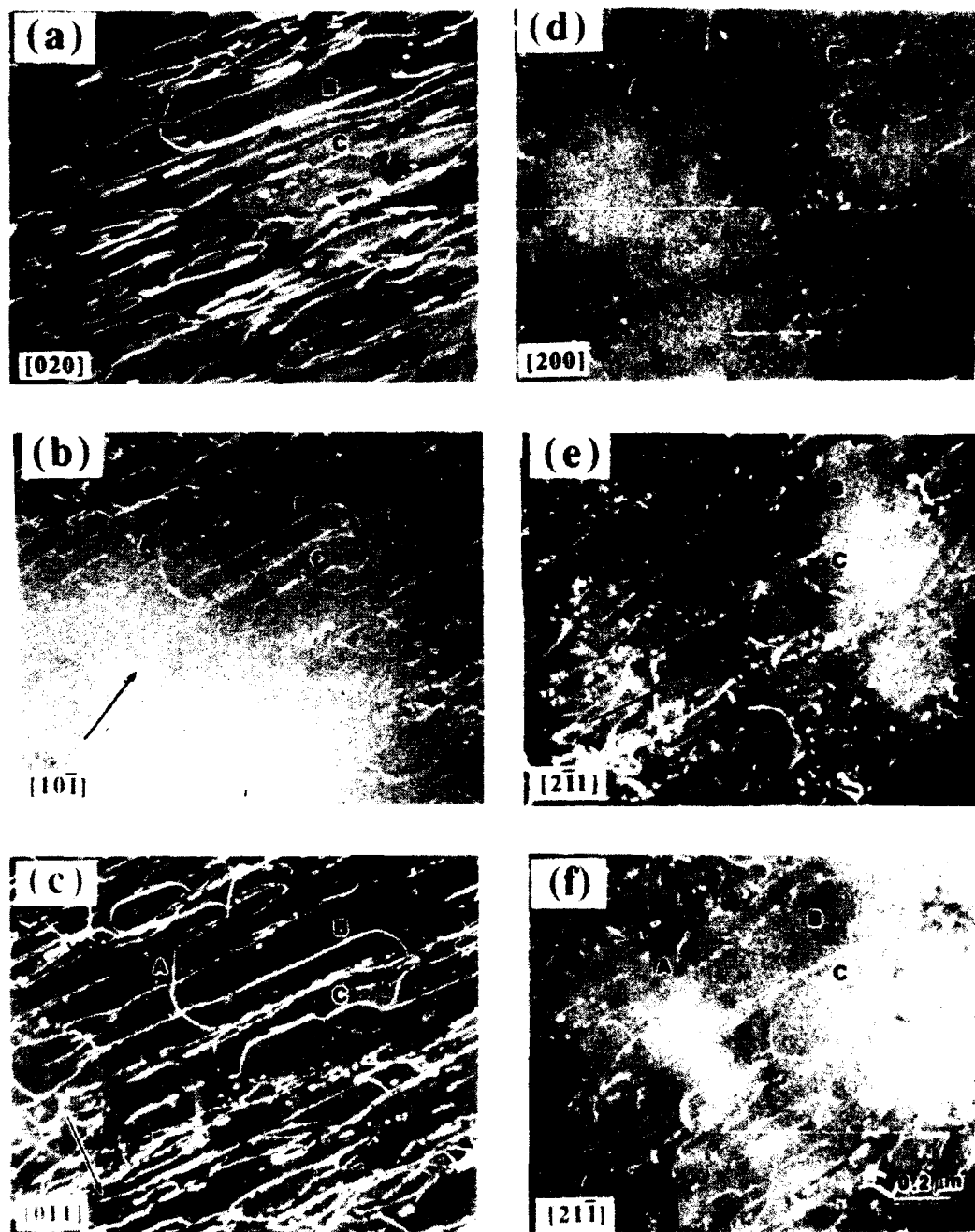
Figure 23   WB micrographs of a **g·b** analysis of dislocations in [232]-A11 deformed
1.6% at 660 °C. Dislocations A-C are edge dislocations with **b**=[011] and **u**=[100], and
lie parallel to the grain boundary. The foil normal is near [0$\bar{1}$1], and the diffraction vectors
are shown.
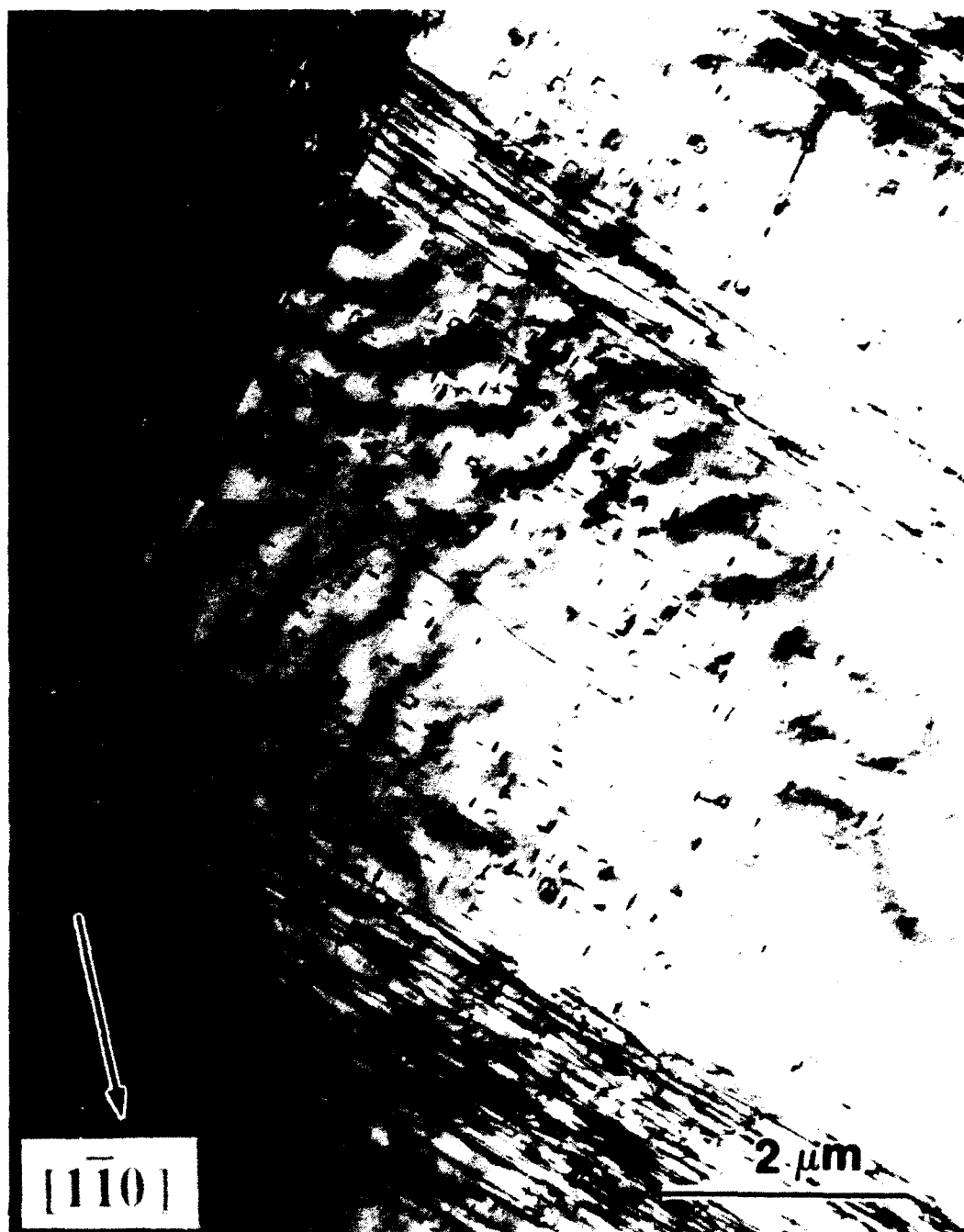
Figure 24   BF micrograph of specimen [353]-A5 deformed 0.5% at 660 °C showing concentrated bands of dislocations and small prismatic loops.

Figure 25   BF micrographs of two intersecting slip bands from crystal A in [353]-A5 deformed 0.5% at 660 °C. Both bands are visible in (a), only b=[100] dislocations are visible in (b), and only b=[010] dislocations are visible in (c). The foil normal is near [001]$_A$, and the diffraction vectors are shown.
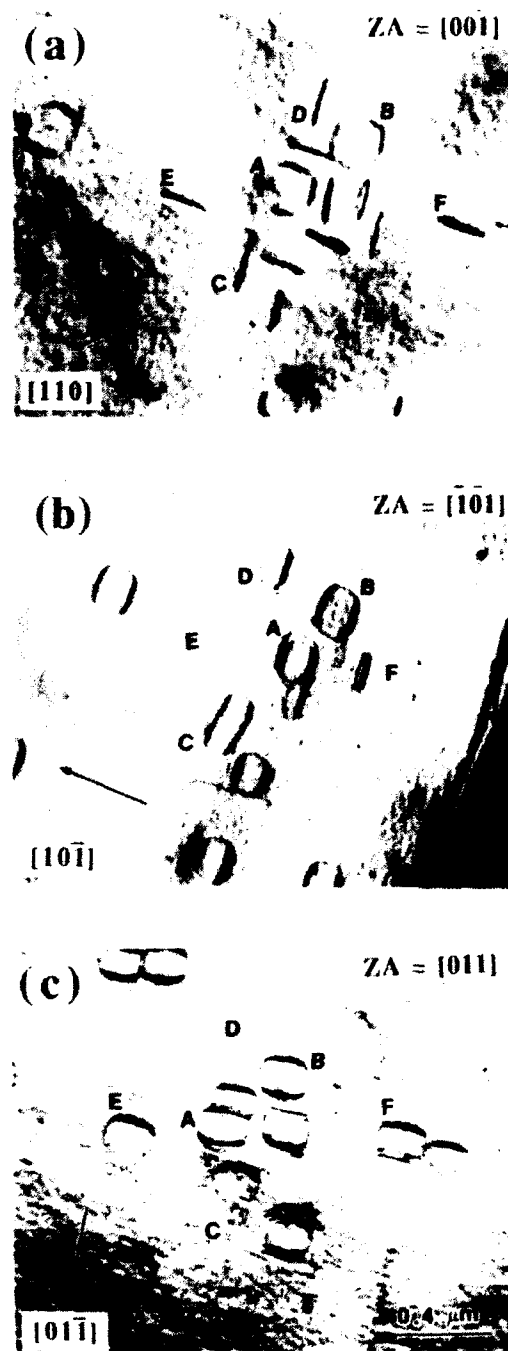
Figure 26   BF images of prismatic loops on {100}$_A$ planes in crystal A from [353]-A5 deformed 0.5% at 660 °C. Dislocation loops A and B are b=[001], loops C and D are b=[100], and loops E and F are b=[010]. The foil normal is near [001]$_A$, and the diffraction vectors and zone axes are shown.

straight and showed very little evidence of curvature, and therefore the plane in which the dislocations were moving could not be determined. Only at intersections of two bands were the dislocations seen to possess significant curvature.

A high density of small, prismatic loops was also seen in foils taken from the $(001)_A$ plane (Fig. 24). Several of these loops are shown in Fig. 26 at a higher magnification. In Fig. 26(a), the dislocation loops labeled A and B are imaged with the plane of the loop normal to the $[001]_A$ zone axis, and the other four loops labeled are viewed end-on. When the foil is tilted 45° toward the $[100]_A$ zone axis, loops A and B appear constricted in the direction parallel to the tilt direction, as expected (Fig. 26(b)). Further, loops C and D are no longer viewed end-on, and are seen as elongated loops. Loops E and F are still viewed end-on, but they are invisible since these are $b=[010]$, and $g \cdot b$ is zero for the diffraction vector used. When the specimen is tilted 45° from the $[001]_A$ axis toward the $[010]_A$ axis, the image of loops A and B are once again consistent with a loop on the $(001)_A$ plane, and loops E and F appear as elongated loops consistent with an $(010)_A$ habit plane. Dislocation loops C and D are viewed end-on, as expected for loops on the $(100)_A$ plane. Therefore, these are all prismatic loops which occur on each of the three $\{100\}$-type planes.

CHAPTER VII

DISCUSSION

7.1 Comparison of Slip Trace and TEM Results

The observation of $(101)_B$ as the active slip plane and $[010]_B$ as the primary slip vector is consistent with the slip system expected to operate for the orientation of crystal B in the bicrystal specimens. Similarly, the TEM observation of the $[01\bar{1}]$ slip vector in crystal A deformed at RT is consistent with the observation of slip markings on the $(010)_A$ face, but not on the $(100)_A$ face. Finally, the slip planes measured by two-surface slip trace analyses are consistent with the Burgers vector observed in the TEM investigations in every bicrystal sample. All of the evidence presented therefore points to the conclusion that $<110>\{110\}$ slip is the dominant mode of deformation in crystal A near the bicrystal interface at RT and 660 °C. This is the first time that the glide of $<110>$ dislocations has clearly been established to occur NiAl. This finding is significant since it constitutes the first unambiguous evidence that the glide of non-$<100>$ dislocations may contribute to the plasticity of polycrystalline NiAl in a general sense, and not only in cube-oriented single crystals where $<100>$ slip is geometrically restricted. Note that even though $<110>\{110\}$ slip is observed only in crystal A, which is in the "hard" orientation, these $<110>$ dislocations become active at essentially the same macroscopically-applied stress required to nucleate $<100>\{110\}$ dislocations in "soft" single crystals or polycrystals, which is far below the stress required to move $<111>$ dislocations in "hard" single crystals.

It would be tempting to speculate, then, that polycrystalline ductility in NiAl may be adequately explained by the occurrence of $<110>$ slip, in addition to the other slip modes available. However, the bicrystals produced and tested were selected to maximize the

82

possibility of inducing non-<100> slip in crystal A, and the generality of this mode of deformation has not been established by this study, as discussed in Section 3.2.1. Careful TEM characterization of polycrystalline NiAl deformed under controlled conditions of temperature and strain rate are required to establish the generality of this mode of deformation. This is clearly an area of future research.

7.2 Nucleation and Movement of <110> Dislocations

The Schmid factor for <111>{110} slip observed in "hard" single crystals is 0.408, while the Schmid factor for <110>{110} slip is 0.5. Therefore, it is clear that the critical resolved shear stress for <110>{110} slip is at least 22% higher than the critical resolved shear stress required to activate <111>{110} slip, even though the <110> dislocations might be presumed to dominate the deformation of "hard" crystals due to their lower elastic energy and smaller Burgers vector. A physical basis for the higher Peierls barrier for <110> dislocations has been suggested by Lautenschlager et al. [68]. Based on a hard sphere model of slip in NiAl, these authors show that the displacement of atoms normal to the {110} slip plane is largest for a <110> slip direction in NiAl when compared to the normal displacements for <100> and <111> unit dislocations. Further, it can easily be visualized that like atoms must come in contact with one another for <110>{110} slip, unlike competing slip translations. The results of the calculations in Table 2 and Table 3 show that the resolved shear stress on the most favored <110>{110} slip system is only 22% higher than the most favored <111>{110} slip system. It is puzzling, therefore, that <110> slip is observed in the deformed bicrystals rather than <111> slip typically observed in deformed "hard" crystals.

It may be possible that <111> dislocations are responsible for deformation in crystal A, and that these dislocations dissociate to <110> and <100> dislocations. As mentioned above, <111> dislocations are the observed dislocations in cube-oriented single crystals, and the dissociation to <110> and <100> is energetically favorable for <111>

edge dislocations, as shown in Fig. 17. However, <111> screw dislocations are not expected to dissociate, and <111> screw dislocations are not observed in crystal A, even in loops where a screw segment must occur. Also, if such a dissociation did occur, then some amount of [100] dislocation debris is expected to remain in crystal A, yet no such dislocations were observed. Finally, if <111> edge dislocations dissociated to [100] and [011] dislocations, then the line direction of the [011] dislocation should be along the $[\bar{2}1\bar{1}]$ direction. However, the [011] dislocations observed typically occur along the [100] direction. The dissociation of a $[11\bar{1}]$ dislocation which lies along the [100] direction to a [100] screw dislocation and an $[01\bar{1}]$ edge dislocation shows no net reduction in line energy, and so is not considered to be a favored reaction. Therefore, the possibility that the dislocations nucleate and move as <111> dislocations, but then dissociate, is not considered likely.

While the critical resolved shear stress for <110> slip is higher than the critical resolved shear stress for <111> slip at RT, as just discussed, the temperature dependence of these parameters is not clear. Above 300 °C, <100> dislocations become mobile before either <110> or <111> dislocations, and so the relative magnitudes of $\tau_{crss}^{<110>}$ and $\tau_{crss}^{<111>}$ are not known. Therefore, it is possible that $\tau_{crss}^{<110>}$ is lower than $\tau_{crss}^{<111>}$ above 300 °C. Although this possibility is consistent with the observed preference for <110> slip at 660 °C, it does not explain the occurrence of <110> slip at RT. Further, if $\tau_{crss}^{<110>}$ is lower than $\tau_{crss}^{<111>}$ above 300 °C, then a source of <110> dislocations needs to be considered. Several possible sources for <110> dislocations are discussed below.

Deformation during the diffusion bonding operation may be expected to result in a high density of <100> dislocations in crystal A near the grain boundary, which may react to form elastically stable <110> dislocation segments. These <110> dislocation segments may then act as sources for <110> dislocations during subsequent deformation. It is possible that these <110> dislocation segments exist, even though they were not observed in foils from the as-bonded bicrystal, since an exhaustive search for their existence was not

carried out close to the bicrystal boundary. All three <100> dislocation types were observed in the as-bonded bicrystal, and it is therefore reasonable to assume that each of the possible <110> dislocations is equally likely to form. However, in each particular bicrystal, only one type of <110> dislocation was observed, and this implies that even if this mechanism does occur, it does not account for the bulk of the <110> dislocations generated.

The transmission of <100> dislocations in crystal B through the grain boundary is another possible mechanism for the introduction of the observed <110> dislocations in crystal A. Due to the difference in magnitude of the <100> and <110> Burgers vectors, roughly two <110> dislocations may be formed in crystal A for every three <100> dislocations in crystal B. Each <110> dislocation emitted in crystal A is expected to possess the same value for b, specifically, the particular <110> dislocation that is best aligned with the [010] dislocations in crystal B may be expected to dominate. These dislocations are expected to move away from the interface as they accommodate the stress at the grain boundary. However, observations in the TEM clearly show that dislocation segments are bowed both toward and away from the grain boundary (recall that the observed slip plane intersects the grain boundary along the $[100]_A$ direction, which is parallel to the long, straight dislocation segments). Therefore, although the transmission of dislocations through the grain boundary cannot be ruled out, some other mechanism must also be considered for the nucleation of <110> dislocations in crystal A.

The final possibility considered is that <110> dislocations may nucleate as loops in crystal A. As for the transmission of dislocations through the grain boundary, each loop formed is expected to have the same Burgers vector. The Burgers vector is constant around each loop, but the line direction will vary around the loop. Therefore, the loop will grow in response to a given state of stress, that is, dislocation segments opposite one another in a given loop will move in opposite directions. The frequent occurrence of loops, which are often elongated along the $[100]_A$ direction (for example, see the loops in

Fig. 22(a) and along dislocations B and C in Fig. 21(c)) supports the suggestion that <110> dislocations nucleate as loops in crystal A. Also, examination of the micrographs in Fig. 21-Fig. 23 shows that segments in the slip plane are bowed both toward and away from the grain boundary. Therefore, it is reasonable to conclude that the nucleation of <110> dislocation loops in crystal A accounts for a significant fraction of the observed dislocations.

Although small, often elongated, <110> loops were frequently observed, larger loops were never observed to be wholly contained in the foil, which is parallel to the slip plane. This implies that some amount of cross-slip or climb of the <110> dislocations may be occurring. An approximate line vector determination of the long segments of dislocation debris sometimes observed after deformation at 660 °C indicates a direction not contained within the slip plane, and this is consistent with the suggestion that some amount of dislocation cross-slip or climb occurs. Some small amount of dislocation climb may also be important in the small rotations (less than 2°) of the <100> dislocations at the grain boundary before being emitted as <110> dislocations in crystal A.

The most stable configuration for a <110> dislocation on a {110} plane at 660 °C is in the screw orientation (Fig. 17). However, edge dislocations dominate the microstructure in crystal A, and these dislocations must therefore be far less mobile than the screw segments. This is corroborated by the observation that the edge segments do not bow out in the slip plane in a direction normal to the interface. Therefore, the motion of the edge dislocation segments away from the interface must occur by some other mechanism. One possibility is that a large double kink forms on the edge segment, and the screw segments thus formed glide along the length of the dislocation, resulting in a displacement of the edge dislocation normal to the bicrystal interface. Dislocation segments which possess a large double kink are relatively common, and are seen in Fig. 21, along dislocation A in Fig. 22, and on dislocation C in Fig. 23.

The dislocation density in crystal A after deformation at RT is significantly lower than after the same amount of deformation at 660 °C. This is consistent with the earlier suggestion that $\tau_{crss}^{<110>}$ decreases rapidly at higher temperatures. Therefore, slip would become active in crystal A at a lower strain level in crystal B, and therefore more of the deformation imposed on the bicrystal will be transmitted to crystal A.

7.3 Deformation in Crystal A by <100> Dislocations

Deformation in crystal A far (>2 mm) from the grain boundary is clearly dominated by the motion of <100> dislocations, even though a macroscopic shear stress does not act on these dislocations. Further, the glide of <100> dislocations cannot produce the imposed strain along the $[001]_A$ axis in crystal A. These observations therefore strongly suggest that the climb of <100> dislocations is responsible for some amount of deformation in crystal A far from the grain boundary.

Since the <100> dislocations observed cannot move by glide, a calculation of the climb force on these dislocations is considered. The Peach-Koehler force on a general dislocation [69] may be written as

$$F/L = (B_2u_3-B_3u_2)i+(B_3u_1-B_1u_3)j+(B_1u_2-B_2u_1)k \qquad (22)$$

where

$$B_1 = b_1\sigma_{11}+b_2\sigma_{12}+b_3\sigma_{13} \qquad (23\ a)$$

$$B_2 = b_1\sigma_{21}+b_2\sigma_{22}+b_3\sigma_{23} \qquad (23\ b)$$

$$B_3 = b_1\sigma_{31}+b_2\sigma_{32}+b_3\sigma_{33} \qquad (23\ c)$$

For uniaxial compression or tension along the [001] axis, $\sigma_{33}=\sigma$, and all other $\sigma_{ij}=0$. Therefore, $B_1=B_2=0$, and $B_3=b_3\sigma$, so that Eqn. (22) above becomes

$$F/L = b_3\sigma[(u_2)i+(u_1)j] \qquad (24)$$

As expected, a climb force exists only on dislocations with a non-zero component for b_3, and the climb force will occur only along directions in the (001) plane. Therefore, only the climb of dislocations with b=[001] and u=[100] or u=[010] is predicted to result from a

87

uniaxial stress along the [001] axis in crystal A.

From this analysis, the climb of the [001] prismatic loops may occur in response the applied stress. However, assuming that these are vacancy edge loops, which is consistent with the sense of the stress applied to the bicrystals, then these loops will act as vacancy sinks, and a source of vacancies is required for extensive motion of these loops. The equilibrium concentration of vacancies in NiAl can be quite high [70], and the chemical potential of these vacancies will increase in the presence of a compressive stress. The equilibrium concentration of vacancies is therefore expected to decrease in the presence of a compressive load, and this supersaturation may provide the vacancies for the nucleation of the small prismatic loops observed. However, even if the entire concentration of equilibrium vacancies (a concentration of $\sim 10^{-3}$ at 1300 °C [70]) could be precipitated as loops, this could not account for the continued, extensive climb of [001] dislocations observed.

An alternate mechanism for a source of vacancies is the climb of [100] and [010] edge dislocations. The extra half-planes of these dislocations would be required to grow in order to accommodate the applied normal strain, and the climb of these dislocations would therefore provide a continuous source of vacancies. The driving force for the motion of the [100] and [010] dislocations may due to the gradient in the chemical potential of vacancies which occurs after some amount of climb of [001] dislocations. This is consistent with the model developed for the climb of dislocations by Nabarro [39], and is also consistent with the observation of [100] and [010] dislocation bands in crystal A. The absence of bands of [001] dislocations in Fig. 23 may simply be a sectioning effect, since these bands are expected to lie in the $(001)_A$ plane, which is parallel to the plane of the foil. It is therefore possible that the climb of [001] dislocations is coordinated with the climb of [100] and [010] dislocations, and that these dislocations occur in localized bands which are parallel to the cube axes. This postulate is consistent with the microstructures observed (Fig. 23), but TEM foils taken parallel to the $(100)_A$ and $(010)_A$ planes are required to support this

88

more fully. This concept is also consistent with the results of the calculations in Section 3.1, which show that diffusion along dislocation cores is required to account for the applied strain rate.

If the proposal of the coordinated climb of <100> dislocations is to be fully considered, then two additional observations must be addressed. First, the observation of surface slip markings along the $(001)_A$ plane is not expected from the climb of [001] dislocations, since no surface offset results from the climb of these dislocations. However, surface slip markings may certainly be observed if the deformation is sufficiently localized, even if no offset occurs on the plane of observation, as shown by the trace of the intense slip band in Fig. 13(a). Therefore, slip markings should also be apparent along the $(100)_A$ and $(010)_A$ planes, but these markings were not observed. While it is true that approximately half the activity is expected on $(100)_A$ or $(010)_A$ planes compared to the amount of activity on $(001)_A$ planes, some evidence of deformation on the $(100)_A$ and $(010)_A$ planes may still be expected. Finally, the force responsible for the climb of [100] and [010] dislocations has not been identified. Although a gradient in the concentration of vacancies may drive the motion of [100] and [010] dislocations, a program to investigate this possibility more fully is suggested.

The sequence of deformation in crystal A may proceed as follows. Plastic deformation initially occurs in crystal B until slip is nucleated near the grain boundary in crystal A. It is not likely that a significant amount of deformation due to the climb of <100> dislocations occurs near the grain boundary prior to <110> slip in crystal A, since (001) traces are not observed in crystal A in the vicinity of the grain boundary and <100> dislocations are not observed in TEM micrographs in this region. At some point, the climb of <100> dislocations begins in crystal A away from the grain boundary. The relative magnitudes of the strain rates which occur in each section of the bicrystal are not known. However, it may be speculated that the strain rate in crystal A away from the bicrystal interface is not very much different from the strain rate due to the glide of <110>

dislocations near the grain boundary in crystal A, since the amount of dislocation activity observed is roughly the same in both regions of crystal A.

CHAPTER VIII

SUMMARY

An examination of the mechanisms proposed for the ductility of polycrystalline NiAl near the ductile-to-brittle transition temperature has shown that the stress-assissted diffusional climb of $<100>$ dislocations cannot fully account for the experimental observations. The available data is consistent with the proposal that glide is the mechanism responsible for the plasticity of this compound at the ductile-to-brittle transition temperature, and the local activation of non-$<100>$ dislocations at NiAl grain boundaries is proposed to account for the observed ductility of this compound. Two bicrystal orientations have been produced to investigate the activation of $<111>$ dislocations due to the concentrated local stress at the bicrystal interface arising from elastic and plastic incompatibility. Observations of surface slip markings and TEM characterization of the dislocations responsible for bicrystal deformation have been made.

The primary conclusion of this study is that the glide of $<110>\{110\}$ dislocations is the dominant mode of deformation in the vicinity of the oriented bicrystal interfaces investigated. More generally, it is concluded that the glide of non-$<100>$ dislocations may contribute to the plasticity of NiAl polycrystals in a general sense, and not just in cube-oriented single crystals where $<100>$ slip is geometrically restricted. The macroscopic stress required to activate these $<110>$ dislocations, in the presence of a stress concentration such as that produced by a dislocation pile-up at a grain boundary, is the same as that required to nucleate $<100>\{110\}$ dislocations, which is far below the stress required to move $<111>$ dislocations in "hard" single crystals. The statistical relevance of this phenomenon as it pertains to the general deformation of NiAl polycrystals has not been

91

established.

A number of possible mechanisms for the nucleation and movement of <110> dislocations have been considered. The only mechanism that may be discounted is that the dislocations move as <111> dislocations and then dissociate into <110> and <100> dislocations. The dominant mode of <110> dislocation generation is reasoned to be the nucleation of <110> loops away from the grain boundary.

Although no resolved shear stress is apparent on <100> dislocations in cube-oriented single crystals, the movement of these dislocations provides the primary mode of deformation in crystals of this orientation far from the bicrystal interface. A climb force due to the applied stress exists on [001] dislocations in a crystal loaded along its [001] axis, but a continuous source of vacancies is required for the extensive motion of these dislocations. It is suggested that the climb of [100] and [010] dislocations provides the required vacancies, and that the gradient in the concentration of vacancies provides the driving force for the motion of these dislocations. The observed dislocation morphology is consistent with this suggestion. The climb of dislocations due to diffusion along dislocation cores is shown to allow for a significant enhancement of the strain rate due to the climb of <100> dislocations.

CHAPTER IX

SUGGESTIONS FOR FUTURE RESEARCH

Two research projects vital to the understanding of the deformation of NiAl are conspicuously absent, and have been discussed in the foregoing investigation. First, a careful TEM study of the operative slip vectors in polycrystalline NiAl after controlled deformation is required to provide a firm basis for the generality of the role of non-<100> dislocations in the plasticity of polycrystalline NiAl. Such an investigation should include the characterization of material that has been processed by both casting (with randomly-oriented grains) and extrusion (to determine the effect of texture). Effort should focus on the behavior near the ductile-to-brittle transition temperature, but a detailed investigation of extruded material exhibiting tensile ductility at RT would also be useful to determine if the mechanism of polycrystalline tensile ductility at RT is related to the mechanism responsible for the ductile-to-brittle transition.

A program to develop a more complete understanding of the mechanism by which cube-oriented single crystals deform above 300 °C is also suggested. It may be considered established that the motion of <100> dislocations is responsible for the deformation of these crystals, yet an understanding of the details are lacking. Critical experiments to determine whether the dislocations move by glide or climb are required. If the dislocations are determined to glide, then the source of the stress to move the dislocations needs to be identified. If these dislocations move by a climb mechanism, then the source of the required vacancies must be verified, along with the driving force for the motion of [100] and [010] dislocations.

REFERENCES

1. C. Zener; in *Elasticity and Anelasticity in Metals*, p. 16, Chicago University Press, Chicago, IL, (1948)

2. R. Darolia, R. Field, and D. Lahrman; *Alloy Modeling and Experimental Correlation for Ductility Enhancement in Near Stoichiometric Single Crystal Nickel Aluminide*, Annual Report, AFOSR Contract F49620-88-C-0052, (1989)

3. J. L. Smialek and R. F. Hehemann; *Metall. Trans.*, **4**, 1571, (1973)

4. R. B. Campany, M. H. Loretto, and R. E. Smallman; *J. of Microscopy*, **98**, 174, (1973)

5. C. H. Lloyd and M. H. Loretto; *phys. stat. sol.*, **39**, 163, (1970)

6. R. J. Wasilewski, S. R. Butler, and J. E. Hanlon; *Trans. TMS-AIME*, **239**, 1357, (1967)

7. A. Ball and R. E. Smallman; *Acta Metall.*, **14**, 1349, (1966)

8. R. T. Pascoe and C. W. A. Newey; *Metal Sci. J.*, **2**, 128, (1968)

9. D. Lahrman, R. Field, and R. Darolia; Unpublished research, (1989)

10. R. Bowman, R. Noebe, and R. Darolia; NASA Conference Pub. 10039, 47-1, (1989)

11. R. T. Pascoe and C. W. A. Newey; *phys. stat. sol.*, **29**, 357, (1968)

12. A. Ball and R. E. Smallman; *Acta Metall.*, **14**, 1517, (1966)

13. M. H. Loretto and R. J. Wasilewski; *Phil. Mag.*, **23**, 1311, (1971)

14. A. Lasalmonie, M. J. Lequeux, and P. Costa; in *Strength of Metals and Alloys*, Proceedings Fifth International Conf., Vol. 2, p. 1317, Pergamon Press, New York, NY, (1979)

15. P. Georgopoulos and J. B. Cohen; *Acta Metall.*, **29**, 1535, (1981)

16. R. de Ridder, G. Van Tendeloo, and S. Amelinckx; *phys. stat. sol. (a)*, **43**, 133, (1977)

17. R. J. Wasilewski; *J. Phys. Chem. Solids*, **29**, 39, (1968)

18. H. L. Fraser, R. E. Smallman, and M. H. Loretto; *Phil. Mag.*, **28**, 651, (1973)

19. H. L. Fraser, R. E. Smallman, and M. H. Loretto; *Phil. Mag.*, **28**, 667, (1973)

20. E. M. Grala; in *Mechanical Properties of Intermetallic Compounds*, (ed. J. H. Westbrook), p.358, John Wiley & Sons, Inc., New York, NY, (1959)

21. C. C. Law and M. J. Blackburn; *Rapidly Solidified Lightweight Durable Disk Materials*, AFWAL TR-87-4102, Air Force Wright Aeronaut. Lab., (1987)

22. E. T. Stover; *Effects of Alloying and Deformation Processing on Mechanical Behavior of NiAl*, WADC-TDR-60-184, Part VII, Vol. II, USAF Contract AF-33(615)-1497, Wright Air Development Center, (1966)

23. A. G. Rozner and R. J. Wasilewski; *J. Inst. Metals*, **94**, 169, (1966)

24. K. H. Hahn and K. Vedula; *Scripta Metall.*, **23**, 7, (1989)

25. E. P. Lautenschlager, D. A. Kiewit, and J. O. Brittain; *Trans. TMS-AIME*, **233**, 1297, (1965)

26. E. P Lautenschlager, T. C. Tisone, and J. O. Brittain; *phys. stat. sol.*, **20**, 443, (1967)

27. S. V. Raj, R. D. Noebe, and R. Bowman; *Scripta Metall.*, **23**, 2049, (1989)

28. E. M. Schulson and D. R. Barker; *Scripta Metall.*, **17**, 519, (1983)

29. E. P. George and C. T. Liu; submitted to J. Mater. Res.

30. P. S. Khadkikar, G. M. Michal, and K. Vedula; *Metall. Trans.*, **21A**, 279, (1990)

31. C. T. Liu, E. H. Lee, and C. G. McKamey; *Scripta Metall.*, **23**, 875, (1989)

32. N. J. Zaluzec and H. L. Fraser; *Scripta Metall.*, **8**, 1049, (1974)

33. I. Baker and E. M. Schulson; *Metall. Trans.*, **15A**, 1129, (1984)

34. P. R. Munroe and I. Baker; *Scripta Metall.*, **23**, 495, (1989)

35. A. Lasalmonie; *J. Mat. Sci.*, **17**, 2419, (1982)

36. R. von Mises; *Z. Angew. Math. Mech.*, **8**, 161, (1928)

37. G. W. Groves and A. Kelly; *Phil. Mag.*, **19**, 977, (1969)

38. H. L. Fraser; PhD Dissertation, University of Birmingham, (1972)

39. F. R. N. Nabarro; *Phil. Mag.*, **16**, 231, (1967)

40. A. E. Berkowitz, F. E. Jaumont, and F. C. Nix; *Phys. Rev.*, **95**, 1185, (1954)

41. R. J. Wasilewski; *Acta Metall.*, **15**, 1757, (1967)

42. G. F. Hancock and B. R. McDonnell; *phys. stat. sol. (a)*, **4**, 143, (1971)

43. N. Rusovic and H. Warlimont; *phys. stat. sol. (a)*, **44**, 609, (1977)

44. W. M. Young and E. W. Elcock; *Proc. Phys. Soc. (London)*, **89**, 735, (1966)

45. A. B. Kuper, D. Lazarus, J. R. Manning, and C. T. Tomizuka; *Phys. Rev.*, **104**, 1536, (1956)

46. H. B. Huntington; *Acta Metall.*, **9**, 749, (1961)

47. J. Weertman; *J. Appl. Phys.*, **28**, 1185, (1957)

48. W. D. Nix and B. Ilschner; in *Strength of Metals and Alloys*, Proceedings Fifth International Conf., Vol. 3, p. 1503, Pergamon Press, New York, NY, (1979)

49. D. F. Stein, in *Dislocation Dynamics*, (eds. A. R. Rosenfield, G. T. Hahn, A. L. Bement, and R. I. Jaffee), p. 453, McGraw-Hill Book Co., New York, NY, (1968)

50. R. R. Vandervoort, A. K. Mukherjee, and J. E. Dorn; *Trans. ASM*, **59**, 930, (1966)

51. W. J. Yang and R. A. Dodd; *Metal Sci. J.*, **7**, 41, (1973)

52. J. Bevk, R. A. Dodd, and P. R. Strutt; *Metall. Trans.*, **4**, 159, (1973)

53. G. M. Rowe, J. Ingram, and P. R. Strutt; Proceedings, 29th Annual EMSA Meeting, p.118, (1971)

54. J. D. Livingston and B. Chalmers; *Acta Metall.*, **5**, 322, (1957)

55. R. E. Hook and J. P. Hirth; *Acta Metall.*, **15**, 535, (1967)

56. R. D. Noebe and R. Gibala; *Scripta Metall.*, **20**, 1635, (1986)

57. G. W. Groves and A Kelly; *Phil. Mag.*, **89**, 877, (1963)

58 P. B. Hirsch, A. Howie, R. B. Nicholson, D. W. Pashley, and M. J. Whelan; in *Electron Microscopy of Thin Crystals*, Butterworths, London, (1967)

59. J. R. Stephens; in *High-Temperature Ordered Intermetallic Alloys*, (eds. C. C. Koch, C. T. Liu, and N. S. Stoloff), MRS Symp. Proceedings, Vol. 39, Pittsburg, PA, p. 381, (1984)

60. J. Demarquay; *C. R. Acad. Sci., Paris*, **220**, 81, (1945)

61. J. F. Nye; in *Physical Properties of Crystals*, p. 131, Clarendon Press, Oxford, England, (1957)

62. J. W. Edington; in *Practical Electron Microscopy in Materials Science*, Vol. 3, p. 14, Philips Tech. Lib., Universities Press, Belfast, N. Ireland, (1975)

63. D. J. H. Cockayne; in *Diffraction and Imaging Techniques in Material Science*. (eds. S. Amelinckx, R. Gevers, and J. van Landuyt), p. 158, North Holland Pub. Co., (1978)

64. D. J. H. Cockayne; *Z. Naturforsch*, 27a, 452, (1972)

65. D. M. Dimiduk, PhD Dissertation, Carnegie-Mellon Univ., (1989)

66. H. L. Fraser; Private communication, (1990)

67. M. H. Loretto and R. E. Smallman; in *Defect Analysis in Electron Microscopy*, pp. 63-66, John Wiley and Sons, New York, NY, (1975)

68. E. P. Lautenschlager, T. Hughes, and J. O. Brittain; *Acta Metall.*, 15, 1347, (1967)

69. M. O. Peach and J. S. Koehler; *Phys. Rev.*, 80, 436, (1950)

70. A. Ball and R. E. Smallman; *Acta Metall.*, 16, 233, (1968)